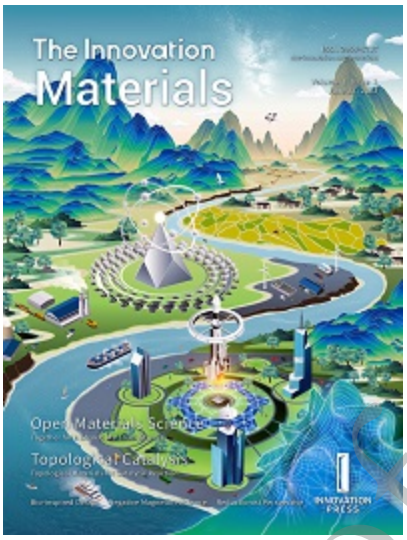

Thermal condensation drives molecular evolution of biochar-derived dissolved organic matter for heavy metal immobilization

Journal:	*The Innovation Materials*
Manuscript ID	TIMS-2026-0019.R2
Manuscript Type:	Article
Keywords:	BDOM, Biochar, Molecular evolution, heavy metal immobilization, High resolution mass spectroscopy

Thermal condensation drives molecular evolution of biochar-derived dissolved organic matter for heavy metal immobilization

Yu Li [1, 3], Xianghui Meng [2, 3], Shuang Ai [2, 3], Markus Antonietti [4*], Fan Yang[1, 3*], Kui Cheng[2, 3*]

[1] College of Hydraulic Science and Engineering, Northeast Agricultural University, Harbin 150030, China.

[2] College of Agricultural Equipment and Energy Engineering, Northeast Agricultural University, Harbin 150030, China.

[3] International Cooperation Joint Laboratory of Health in Cold Region Black Soil Habitat of the Ministry of Education, Harbin 150030, China.

[4] Department of Colloid Chemistry, Max Planck Institute of Colloids and Interfaces, Potsdam 14476, Germany.

*Correspondence: chengkui@neau.edu.cn (K.C.); yangfan_neau@163.com (F.Y.); office.cc@mpikg.mpg.de (M.A.)

* Corresponding author.
Prof. Kui Cheng, chengkui@neau.edu.cn
Prof. Fan Yang, yangfan_neau@163.com
Prof. Markus Antonietti, office.cc@mpikg.mpg.de

GRAPHICAL ABSTRACT

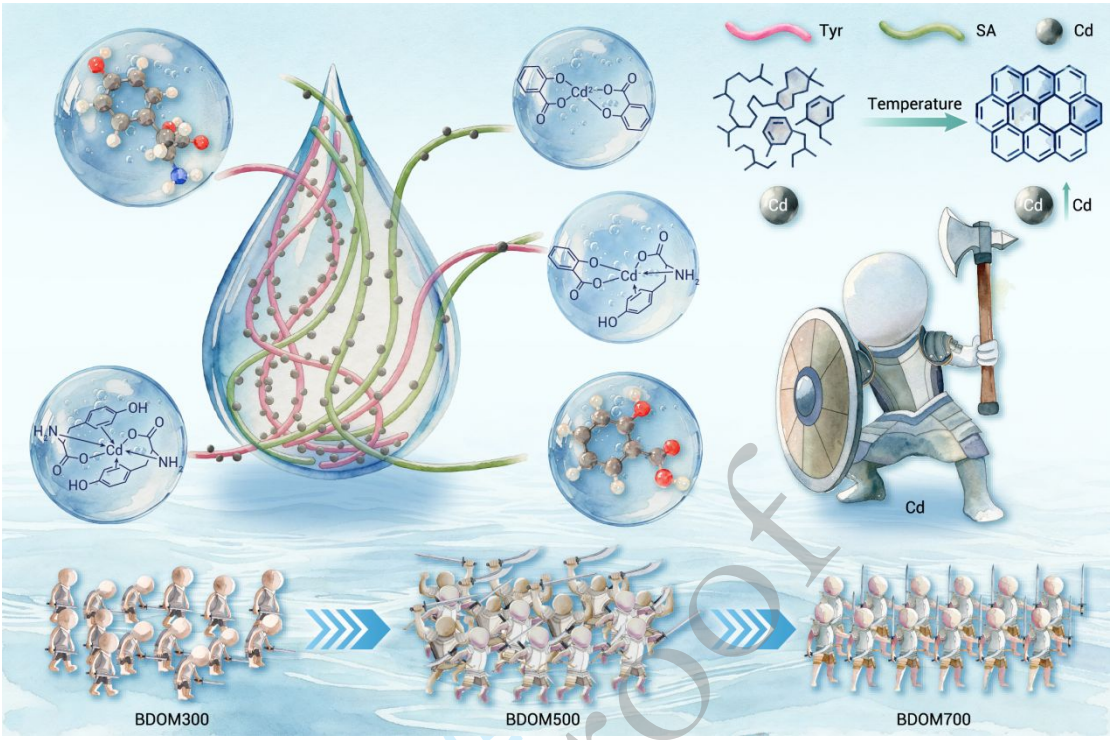

PUBLIC SUMMARY

- BDOM was identified as an important determinant of biochar-mediated Cd binding in soils.
- Thermal reorganization throughout the charring process shifts BDOM from heterogeneous humic aggregates to phenolic, O-coordinating domains.
- This reorganization enhances Cd immobilization and limits the transfer from the soil to the biosphere, here ryegrass

ABSTRACT

Biochar-derived dissolved organic matter (BDOM), the soluble fraction of biochar, plays an important yet underrecognized role in environmental chemistry, here exemplified by heavy metal mobilization/immobilization. Current studies largely emphasize biochar as a beneficial additive to soil, but neglect the specific role of the highly functional BDOM. In an integrated approach combining spectroscopic analysis, ultrahigh-resolution mass spectrometry, and reaction network modeling, we show that BDOM is the overlooked reactive fraction in biochar application. The complex condensation-derived molecular structures of BDOM across a range of typical pyrolysis temperatures (300-700℃) was analyzed, and molecular transformations changed by metal coordination were elucidated. We demonstrate that higher pyrolysis temperatures facilitate decomposition of humic aggregates and form tyrosine-like phenolic ligands. Using cadmium (Cd) binding as a model metal-interaction process, we show that low temperature pyrolysis produces soluble condensation products which mobilize Cd, while Cd mobility is strongly reduced by the high temperature pendants. This transformation occurs via coordinative mechanisms involving rearrangement of functional groups, conformational changes in polymer structures, and hydrophobic microencapsulation.

Finally, we demonstrate that the optimized coordination structure significantly suppresses Cd mobility in the environment and especially minimizes plant uptake. Our thermally controlled synthesis sheds a new light on the role of BDOM and provides a rationale for the controversial reports on different biochars in soil applications.

INTRODUCTION

Biochar (BC) is a widely used sustainable class of environmental materials for heavy metal adsorption,[1] where the prevailing mechanistic views attribute its contaminant immobilization to intrinsic properties such as microporous structures, surface charge-driven electrostatic attractions, and metal coordination via oxygen-containing functional groups.[2] However, we will show that this conventional perspective overlooks a liquid-phase component we believe to be critical: coexisting soluble carbon condensates, named biochar-derived dissolved organic matter (BDOM). Recent studies on biomass-derived functional materials have further emphasized that material performance is governed not only by the final solid carbon phase, but also by feedstock chemistry, extractable molecular fractions and thermal processing history.[3-5] Acting as both a contaminant transport vector and reactive interface,[6] BDOM represents a mobile and reactive fraction associated with biochar, modulating metal fluxes disregarded by traditional adsorption models.[7] The scientific significance of BDOM lies in its dual character: it inhered complex chemical structure from pyrolysis, while molecular dispersion amplifies its biogeochemical reactivity.[8]

A fundamental challenge in leveraging BDOM stems from its extreme molecular heterogeneity, where thousands of compounds with distinct redox states, aromaticity, and functionalization can coexist.[9] This complexity complicates characterization and obscures clear structure-function relationships. Conventional analyses reduce this multidimensional chemical landscape to oversimplified proxies (e.g., $SUVA_{254}$ or

average molecular weight),[10] while obscuring the pyrolysis-temperature imprint on BDOM molecular composition.[11] Pyrolysis temperature enables to selectively discriminate between less and more stable bonding moieties and functional group distribution via energy-selective bond cleavage, as well as it promotes aromatic condensation, thereby predetermining BDOM's environmental behavior through conformational legacies.[12]

Despite growing recognition, a significant knowledge gap remains. Mechanistic models remain anchored to static BC-solid interactions, ignoring liquid-phase BDOM-mediated metal redistribution dynamics and neglecting altered condensation cascades caused by metal coordination.[13,14] Thermal effects currently remain empirically analyzed, lacking predictive links between pyrolysis parameters and materials properties.[15]

Here, using Cd as a highly relevant model of a heavy metal contaminant, we interrogate how thermal programs (300-700℃) reconfigure BDOM's molecular architecture in dependence of the presence of metals. Most importantly, using high-resolution mass spectrometry, we are able to determine and characterize more than 7000 components of isolated BDOM fractions. Integrating this with spectral tracking and reaction network modeling, a reaction map of the dynamic trajectories of chemical evolution from oxygen-rich moieties to condensed aromatic domains can be created. This approach delivers a systems-level understanding of BDOM evolution beyond compositional inventories. Finally, by establishing mechanistic links between pyrolysis-driven molecular evolution and environmental functionality, this work

enables a more rational and advanced design of BDOM-based remediation strategies.

MATERIALS AND METHODS

BDOM sample preparation

The corn stover were selected as raw materials for preparing BDOM. They were collected from Heilongjiang Province, China and dried at 30℃ for 24 h to reach a constant mass, ground into powder using a high- speed pulverizer, and passed through a 60-mesh sieve. The proximate and elemental compositions of the pretreated corn stover were determined before pyrolysis and are summarized in Table S1. The pretreated corn stover powder was pyrolysed under a N_2 atmosphere at a heating rate of 15 ℃/min to 300, 500 or 700℃, and each target temperature was maintained for 2 h. The resulting biochars were used to prepare BDOM300, BDOM500 and BDOM700.

10 g biochar was added into deionized water (200 mL) and sonicated in the ultrasonic bath for 0.5 h. The biochar suspension was separated by centrifugation for 0.25 h at 5000 rpm. The obtained supernatants were filtered through a 0.45 μm membrane and used as BDOM stock solutions.[16] According to the biochar feedstock, these BDOM samples are denoted as BDOM300, BDOM500 and BDOM700, respectively.

BDOM-Cd complexation experiments

The binding studies were carried out in amber glass vials with a volume of 40 mL. To stabilize ionic strength, a $NaNO_3$-based background electrolyte solution was introduced, resulting in a nitrate concentration of 0.01 mol/L. The pH was maintained at 7.0 by employing a 10 mM phosphate buffer, which was prepared by mixing KH_2PO_4

and NaOH at a mass ratio of 85.3. Cadmium (Cd) was added to the system at varying levels (0-5 mg/L) to generate a comprehensive binding isotherm for BDOM-Cd interactions. To account for the background effect of the phosphate-buffered matrix on dissolved Cd, BDOM-free controls were prepared using the same Cd concentration gradient and reaction conditions (Table S2). The amount of Cd associated with BDOM was calculated from the difference between the residual Cd concentration in this BDOM-free control and that in the BDOM-containing treatment. The mixtures were continuously shaken at 140 rpm and allowed to equilibrate for 24 h at 25℃ to facilitate complete complexation. Following equilibration, the samples were passed through 0.45 μm filters to eliminate any precipitated solids. To guarantee reproducibility, each experimental condition was tested with a minimum of three replicates.

FT-ICR MS data analysis

The raw spectral data were processed using Data Analysis software (v5.2, Bruker Daltonics, CA), extracting m/z values with a signal-to-noise (S/N) threshold exceeding 7. Experimental mass measurements were internally calibrated using reference compounds listed in Table S3 before molecular formula determination. Putative chemical formulas were derived using the Compound Identification Algorithm (CIA) implemented in the Formularity software. Assignments were constrained to a mass accuracy of ≤ 0.5 ppm within the m/z range of 100-1000. Following established guidelines (golden rules),[17] we considered only C, H, O, N, and S in formula assignments. To enhance reliability, preference was given to formulas with minimal heteroatoms (N, S) and the smallest mass error.[18] A summary of formula assignments

is provided in Table S4. Assigned formulas were grouped into four elemental categories: CHO, CHON, CHOS, and CHONS. Additionally, biochemical classifications-including lipids (LP), proteins/amino sugars (PA), carbohydrates (CH), unsaturated hydrocarbons (UH), lignin (LG), tannins (TN), condensed aromatics (CA), and unclassified compounds ("other")-were assigned based on predefined H:C and O:C ratios (Table S5). These classifications serve as preliminary groupings for data interpretation rather than definitive structural identifications, as MS/MS validation was not performed.

Given the structural complexity of BDOM, computational approaches were employed for characterization. The modified aromaticity index (AI_{mod}) was calculated to estimate aromaticity: AI_{mod}= (1+C-0.5*O-S-0.5*(N+H))/(C-0.5*O-N-S), where C, H, O, N, and S denote atom counts in each formula.[19] The double bond equivalent (DBE) was computed as: DBE=1+C-0.5*H+0.5*N. To assess single C-C bonds, we used the C-1-DBE index, acknowledging potential underestimation due to undifferentiated non-C-C double bonds (e.g., C=O, C=N). The nominal oxidation state of carbon (NOSC) of each organic molecule was calculated using the following equation: NOSC=-H/C+2*O/C+3*N/C+2*S/C.[20] Gibbs free energy of a given organic compound can be computed as the standard molar enthalpy of its complete combustion (ΔH). ΔH values are calculated based on the Patel-Erickson equation, where the standard molar enthalpy of combustion of organic matter is proportional to the number of electrons that it transfers to oxygen during combustion.[21,22] This proportionality is expressed through the equation: ΔH=-114.14*(4*C+H-2*O-0*N+6*S)/C.[23] Functional group

transformations (e.g., oxygenation, decarboxylation, dealkylation, deamination, desulfonation) between BDOM and BDOM-Cd samples were quantified. These computations were performed using R.

RESULTS

BDOM molecular composition, distribution, and properties

Biochar samples were prepared from corn stover under a N_2 atmosphere at pyrolysis temperatures of 300, 500 and 700℃. The organic matter conversion rates of biochars produced at the three pyrolysis temperatures were analyzed (Method S1 & Figures S1-2). Higher pyrolysis temperatures led to lower BDOM release and slower release kinetics, which can be attributed to the formation of a more refractory carbon matrix, depletion of oxygen-containing functional groups and ash-derived mineral constraints within the biochar structure (Figures S3-6 & Table S6). During pyrolysis, these inorganic constituents may catalyze dehydration, decarboxylation and deoxygenation reactions, while also forming local mineral-associated barriers that restrict the liberation of soluble organic products.[24] The molecular analysis of all BDOMs identified a core molecular community comprising 1782 molecular formulas shared across all samples (Figure 1A), with LG compounds predominating (75% in BDOM300 and BDOM500, decreasing to 60% in BDOM700) (Figure S7 & Table S5). LP compounds showed a marked increase from 2% in BDOM300 to 6% in BDOM500, while CA and TN substances rose to 21% and 13%, respectively, in BDOM700. All these compounds are predominantly composed of CHON and CHO elements (Figure S8). During the initial pyrolysis stage (300-500℃), hemicellulose and cellulose

underwent selective thermal degradation, and evaporation results in a 29.6% mass loss of the biomass (Figure 1B).[25] Physically adsorbed water and volatile organic compounds are released from biomass through endothermic processes.[26] This leads to the dissolution of the intermolecular water-based hydrogen bond networks, subsequently inducing the liberation of oligosaccharides, acids, ketones, xylose, and other products.[27] These compounds undergo decomposition, and the consecutive aromatic cyclization reactions via aldol reactions and Diels Alder addition/elimination schemes are enhanced. This process ultimately leads to the formation of polyaromatic, oxygen-functional structures in the biochar (Figure 1D).[28] During the carbonaceous solid-phase formation stage (500-700℃), lignin begins to dominate the pyrolysis process.[29] ß-O- linkages are broken to double bonds and phenolic groups, followed by deoxygenation reactions (dehydroxylation, decarbonylation). These transformed compounds subsequently undergo polycondensation to form the condensed aromatic structures (Figure 1C & Table S7). Concurrently, the residual aliphatic side chains underwent chain scission, generating volatile fragments, or crosslinking and further dehydrogenation when unsaturated (Figure 1E), leading to significantly enhanced structural compactness and thermal stability (Table S8). Principal component analysis (PCA) clearly distinguishes the BDOM molecular compositions among the different samples (Figure 1F). Mass distribution analysis of BDOM (Figure S9) revealed a temperature-dependent shift toward higher molecular weight ranges, a phenomenon closely associated with the preferential volatilization of low-MW compounds during pyrolysis,[30] and formation of thermally stable, condensed aromatic structures through

dehydrogenation and deoxygenative cyclization.[31]

The degree and type of oxygen functionalization plays a crucial role in metal coordination and is significantly influenced by pyrolysis temperature.[32] Here, we used the standard molar combustion enthalpy (kJ/mol C) as an approximation for the Gibbs free energy associated with the complete oxidation of a given organic compound. This allowed us to assess the dependence of molecular energy potential on the nominal oxidation state of carbon (NOSC).[30,33] Notably, a strong linear relationship is observed between the average combustion enthalpy (ΔH) and NOSC values of each compound classes ($R^2 = 0.96679$) (Figure 1G). During BDOM transformation, most compound classes show an increasing ΔH and NOSC values from BDOM300 to BDOM700 (Table S9), demonstrating that pyrolysis mostly splits off water and oxidized carbon species, leaving C-C bonding behind. As a consequence, the relative carbon content increases with carbonization temperature. BDOM700 contained a higher proportion of recalcitrant molecules (Table S10). This observation is further supported by the intensity-weighted ΔH-NOSC relationships, where the relative intensity weight serves as the unit of account for each molecule (Figure 1H). The linear decrease in energy density of a broad range of organic substances by 115.78 kJ/mol C per NOSC is supported by experimental data from BDOM300-700 samples, which all show linear ΔH-NOSC relationships within the prediction range of simulated data. Furthermore, molecular clusters of BDOM300 and BDOM500 are predominantly distributed in the negative NOSC region (Figure S10), indicating their composition is dominated by reduced substructures. These low oxidation-state molecules typically exhibit higher

chemical reactivity and tend to be preferentially consumed in environmental matrices through oxidation reactions or ligand competition.[34] In contrast, BDOM700 exhibited significantly positive NOSC values, indicating dominance of aromatic structures formed through dehydrogenative condensation. Their molecular structures confer enhanced chemical stability and environmental resistance to degradation.[35]

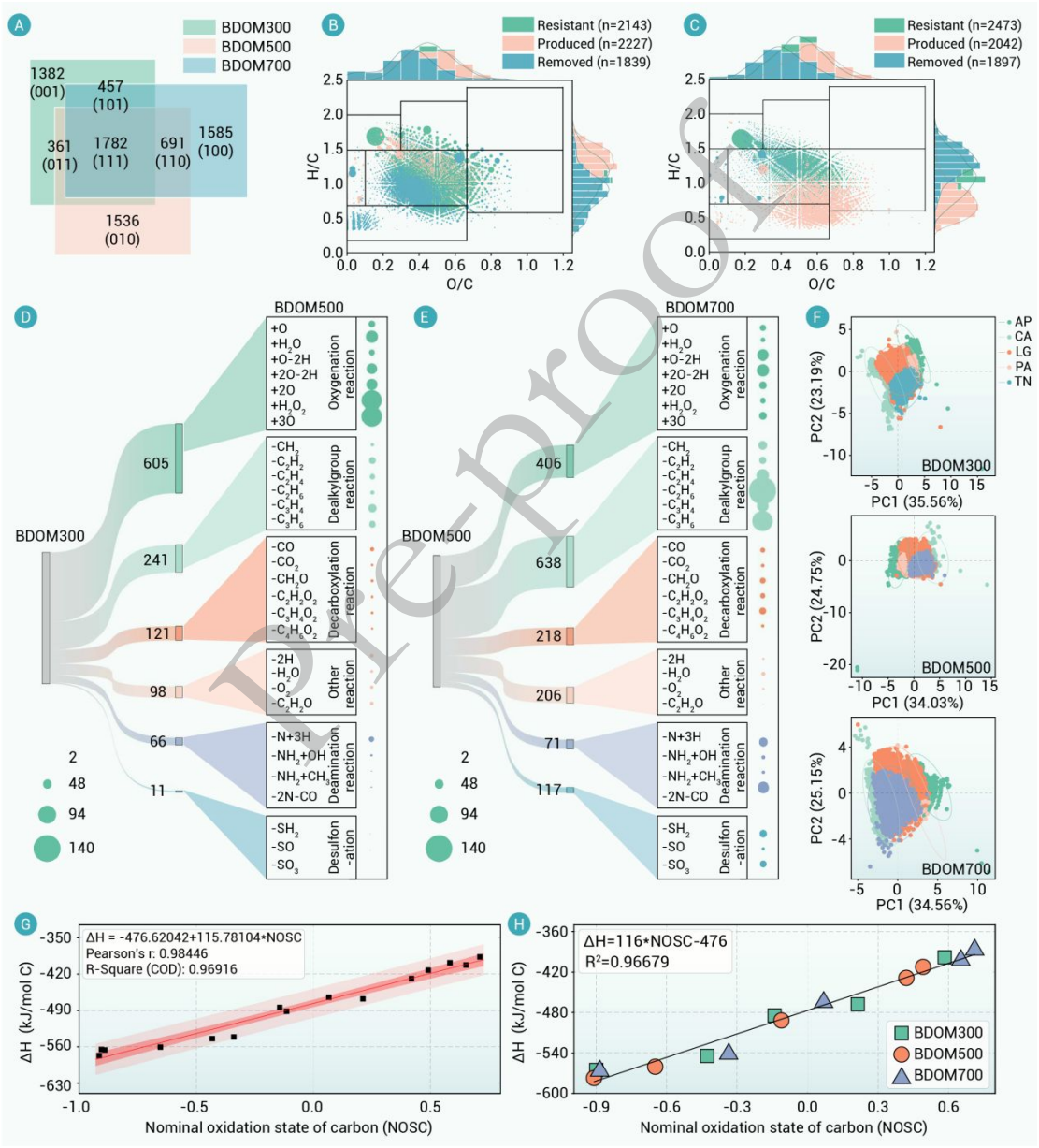

Figure 1 | Comparative analysis of molecular characteristics in BDOM across thermal gradients (A) Venn diagram of molecular distribution in BDOM. (B-C) Van Krevelen diagrams revealed the molecular transformation of BDOM during progressive temperature

elevation. (D-E) Potential Biochemical Transformations in BDOM300-700 and Temperature-Dependent Precursor-Product Relationships. (F) PCA of the relationship between molecular composition and structural factors: H/C ratio, double bond equivalent (DBE), aromaticity index (AI_{mod}) and other relevant parameters. (G) The relationship between average ΔH (kJ/mol C) and NOSC values of compound classes of BDOM300-700. (H) Linear relationship validated using known compounds in BDOM, with the shaded area representing the 95% prediction interval of the fitted linear regression model.

Variations in coordination mechanisms

Metal complexation experiments with these BDOMs showed a clear increase in Cd chelation capacity of BDOM as pyrolysis temperature rose from 300℃ to 700℃ (Figure S11). Topological network analysis indicated that BDOM300 exhibited the highest reactivity for complexation, undergoing significant aggregation, cross-linking, and precipitation, ultimately resulting in denser local structures. BDOM500 and BDOM700 demonstrated improved stability, primarily reflected by increased network modularity and moderate reinforcement in connectivity (Figure 2A). This phenomenon closely correlates with the progressive simplification of component structures and dynamic reorganization of functional group binding sequences.

According to Noda's rules, we further elucidated the temperature-dependent coordination disparities through functional group binding sequences resolved by the synchronous/asynchronous correlation spectra (Figure 2B & Tables S11-14).[36] The binding sequence of BDOM300 (1417 > 1056 > 2961 > 3439 > 567 > 1647 cm^{-1}) reveals that its chelation process initiates with rapid coordination via carboxylate symmetric vibration (1417 cm^{-1}), followed by C-O stretching (1056 cm^{-1}) participating in preliminary complex formation. However, carboxylate groups constitute merely 2%

of total functional groups (Figures S12-13), indicating that while these moieties exhibit high reactivity, their limited absolute abundance restricts overall coordination capacity.

The binding sequence of BDOM500 shifted to 1417 > 2961 > 3439 > 1647 > 1056 > 567 cm^{-1}, featuring earlier involvement of aliphatic C-H vibrations (2961 cm^{-1}). This likely stems from pyrolytically generated short-chain alkyl groups enhancing hydrophobic association, thereby accelerating Cd-organo complex formation. Notably, carboxylate abundance increased to 17%, substantially boosting initial coordination contribution. Aromatic C=C/amide I (1637 cm^{-1}) peak area decreased from 7% to 4%, yet its 1647 cm^{-1} counterpart advanced to 4th in sequence, suggesting condensed aromatic systems in residual humic substances achieve higher π-electron density after thermal treatment, strengthening cation-π interactions with Cd. The binding sequence of BDOM700 shifted to 1056 > 1417 > 3439 > 2961 > 1647 > 567 cm^{-1}, with the C-O band becoming the earliest responding signal and its relative contribution increasing to 37%. This transition reflects a reorganization of oxygen-containing coordination environments during high-temperature pyrolysis. As polysaccharide-derived aliphatic structures were progressively dehydrated and condensed, the remaining C-O signals were more likely associated with phenolic, aryl ether-like and carboxyl-linked oxygen motifs within condensed molecular domains. These reorganized C-O environments reduced the structural disorder of the binding interface and allowed C-O-containing domains to participate earlier in the coordination sequence of BDOM700. Notably, infrared spectra revealed the disappearance of amide I bands at 1650-1655 cm^{-1} (observed in BDOM300, Figure S14) and the emergence of signals at 1620-1635 cm^{-1}

in BDOM500 and BDOM700.[37] This shift signifies reorganization of nitrogenous moieties into conjugated, electron-deficient domains through pyrolytic condensation. These structured domains create microenvironments favorable for metal coordination via chelation and π-electron interactions.

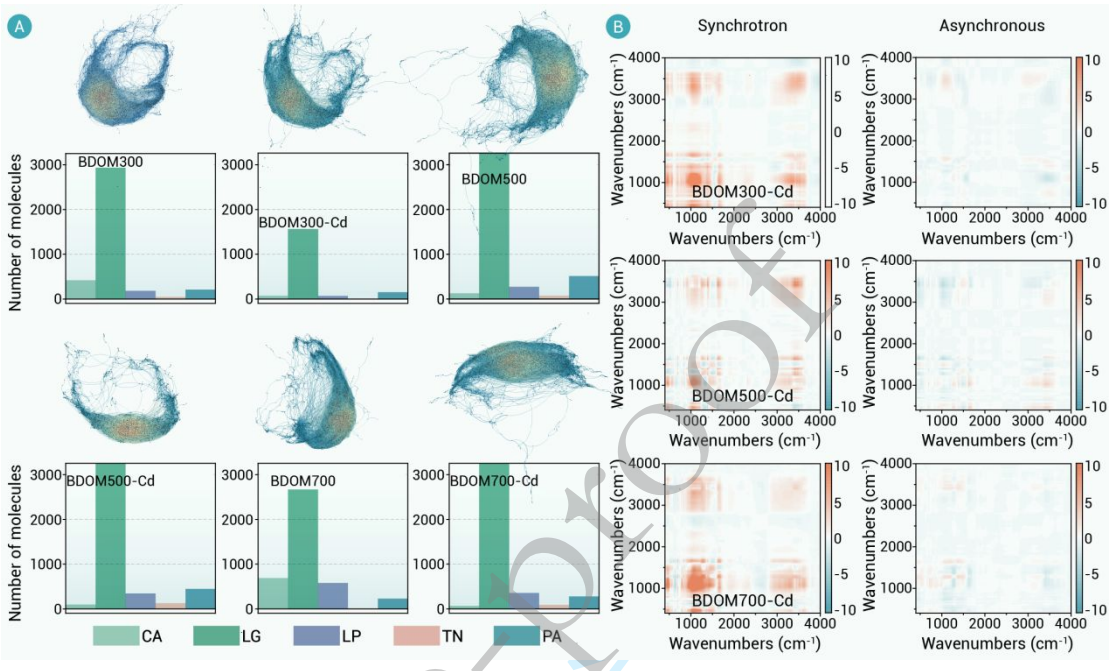

Figure 2 | Thermal reorganization reshapes BDOM molecular networks and Cd coordination pathways (A) Molecular network topology analysis of the BDOM system before and after Cd coordination, along with quantitative changes in compound composition, are presented with detailed parameters in Table S18. (B) 2D-F'TIR-COS synchronous and asynchronous maps of BDOM-Cd complexes, red and blue denote a positive and negative cross-peak, respectively. Darker color demonstrates a stronger positive or negative correlation, The order of signs were showed in Table S13.

EXAFS analysis revealed detailed information about the coordination environment between metals and ligands, including coordination numbers and bond lengths. As shown in Figures 3A-C, the near-edge binding energy of BDOM-Cd

complexes was higher than that of Cd foil, with E_0 consistently around 26713 eV. This observation confirms that no valence change occurred during Cd complexation with BDOM, indicating coordination interaction served as the primary binding mechanism. Compared to BDOM700, BDOM300 and BDOM500 exhibit negative shifts of 0.03 Å and 0.01 Å, respectively, which may be attributed to differences in their electronic structures and coordination environments (Figure S15). Structural parameters derived from Cd K-edge EXAFS fitting data (Table S3) reveal that BDOM-Cd coordination bonds consist of Cd-N, Cd-O, and Cd-S linkages. In the first coordination shell, BDOM500 exhibits the highest Cd-N coordination number (2.40), while BDOM700 shows a significantly increased Cd-O coordination number (1.71). Additionally, BDOM500 displays a prominent Cd-S coordination bond in the second shell. These observations can be ascribed to the abundance of N- and S-containing functional groups (e.g., amine and thiol groups) in BDOM500, which facilitate stronger Cd coordination, leading to higher Cd-N and Cd-S coordination numbers. In contrast, pyrolysis at 700℃ preserves O-containing functional groups (e.g., carboxyl and phenolic hydroxyl groups) in BDOM700, enhancing Cd-O coordination. The stability of Cd complexes varies with the coordination environment. Cd-N and Cd-S coordination in BDOM500 yields stable complexes, whereas Cd-O coordination in BDOM700 forms complexes that are more stable. Further wavelet transform (WT) analysis of the Cd K-edge EXAFS signals (Figure 3D) reveals strong WT signals across all BDOM samples, with intensities matching the oscillation peaks in R-space. Although the similar atomic radii of O, N, and S make it challenging to resolve their individual contributions, the observed

splitting at the edges of the strong signals provides additional evidence for distinct Cd coordination environments. These variations in ligand-specific coordination critically influence Cd chelation behavior.

Parallel factor (PARAFAC) analysis, a robust method for examining BDOM fluorescent properties, provides molecular insights into structural and functional characteristics governing organic-metal interactions (Figures S16-17 & Table S15).[38] Three distinct fluorescent components were identified in BDOM300-Cd, marine-like humic substances (Ex: 235/310 nm, Em: 390 nm), terrestrial humic substances (Ex: 265/350 nm, Em: 450 nm), and tyrosine-like (Tyr) phenols (Ex: 280 nm, Em: 325 nm). The three-dimensional network structure of humic substances may impose steric hindrance effects on Cd, reducing the accessibility of chelation sites.[39] In BDOM500, the number of components decreased to two, previously called "marine-like" humic substances (Ex: 280 nm, Em: 315 nm) and tyrosine-like phenolic sites (Ex: 320 nm, Em: 305/420 nm). This compositional simplification likely mitigates intermolecular competition for chelation, though residual humic substances may still form molecular aggregates via π-π stacking interactions, partially masking active binding sites.[40] Remarkably, BDOM700 fully transforms into structures with three tyrosine-like phenolic binding sites per metal, maximizing chelation sites exposure, consistent with its experimentally confirmed highest Cd uptake. Notably, the disappearance of the 558 cm^{-1} peak (metal-O vibration) in BDOM700-Cd does not indicate loss of coordination capability. Instead, high-temperature pyrolysis facilitates deeper embedding of Cd into the hydrophobic cavities, altering metal-O bond lengths beyond the detection range of

FTIR.[41] This phenomenon aligns mechanistically with the coordination shell reorganization observed in EXAFS studies.

Density functional theory (DFT) calculations were used to further examine the energetic basis of the two major fluorescent ligand environments resolved by PARAFAC. Salicylic acid (SA) was selected as a simplified model for humic-like aromatic carboxyl–phenolic domains, whereas tyrosine (Tyr) was used to represent the Tyr-like phenolic component identified in BDOM700.[42,43] Under near-neutral conditions, phenol synergy directly enables significantly higher binding energy (-38.0 kcal/mol) and dissociation energy (33.3 kcal/mol) than other systems (Figures S18-19 & Table S16). In alkaline environments, although deprotonation elevates monomeric SA binding affinity (-31.6 kcal/mol) above monomeric Tyr (-19.8 kcal/mol) (Figure S20 & Table S17 & Figure 3E), robust ligand cooperativity in the dual-Tyr system (21.2 kcal/mol synergistic energy) bridges this gap. This results in the binding energy (-60.8 kcal/mol) of dual Tyr being comparable to dual-SA (-62.8 kcal/mol) and the mixed-ligand systems (-61.5 kcal/mol). Crucially, the dual-Tyr complex retains high dissociation energy (41.0 kcal/mol), confirming its kinetic stability (Figure 3F). Similarly, the stronger Cd binding of BDOM700 across varying pH conditions may be associated with cooperative coordination by Tyr-like phenolic domains, presumably realized by modified phenolic heterocycles or carboxyphenoles. The enrichment of Tyr-like phenolic components at 700℃ pyrolysis therefore provides a plausible molecular basis for the enhanced metal-binding capacity of BDOM700.

In summary, pyrolysis temperature governs the cadmium immobilization capacity of

BDOM through two pathways: macroscopic component simplification (humic substance condensation and enrichment of phenols, heterocycles, and carboxylates) reduces competitive binding sites, and microscopic functional group reorganization with optimization of binding environments establish spatiotemporally cooperative mechanisms. This hierarchy is visually decoded in Figure 3G through schematic representations of differential coordination regimes-BDOM300 exhibiting competitive steric hindrance in SA ligands, BDOM500 demonstrating isolated non-cooperative binding, while BDOM700 reveals a Tyr-like superior efficacy via geometrically complementary sites enabling cooperative immobilization. The optimized performance at 700℃ pyrolysis originates from three synergistic determinants: abundant C-O groups enabling rapid initial coordination, rigid frameworks providing geometrically aligned carboxylate/phenol chelation sites, and hydrophobic cavity encapsulation conferring intrinsic complex stability.

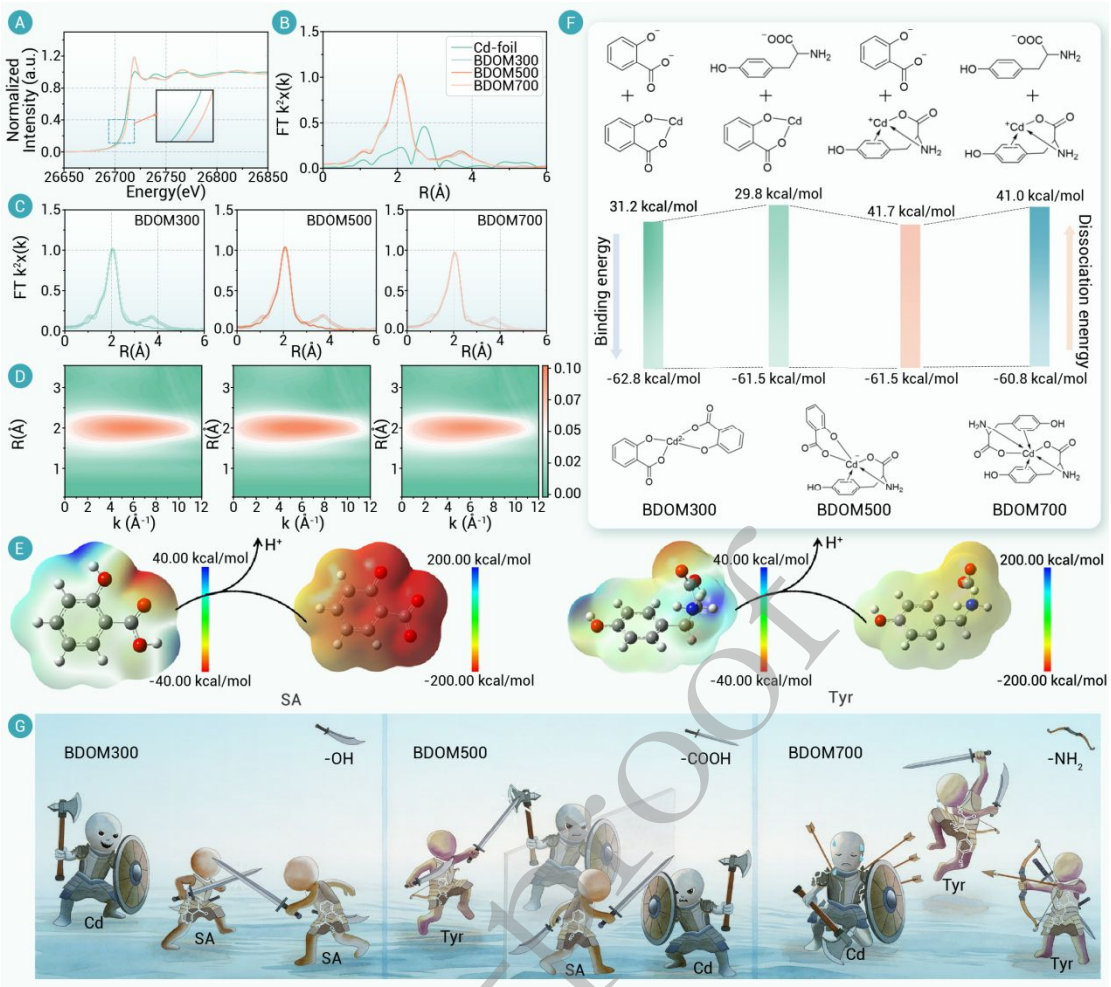

Figure 3 | Structural analysis of BDOM-Cd (A) comparison of Cd K-edge normalized XANES spectra. (B) FT curves of the Cd K-edge EXAFS.(C) Fitting curves of F'T-EXAFS spectra in R space. (D) Wavelet transform of the Cd K-edge. (E) Comparative analysis of electrostatic potential energy surfaces for salicylic acid and tyrosine in both protonated and deprotonated states. (F) Binding energies of Cd in different systems after deprotonation, along with the energies required for dissociating one molecule from the coordination compounds, are presented. Pre-deprotonation binding and dissociation energies are provided in Figures S14-15 for comparison. (G) Schematic diagram of the coordination mechanism between BDOM and Cd, illustrating tyrosine's synergistic role in chelation and the performance advantage of high-temperature-induced protein component enrichment.

Molecular transformation analysis

A major challenge in DOM research is visualizing the potential biological and chemical transformations DOM undergoes over its lifecycle. Quantitative analysis of

molecular transformation pathways and their flux differences also clarifies the temperature-dependent molecular mechanism underlying optimized coordination performance. Under metal coordination, BDOM300 released 1870 molecules primarily consisting of LG, LP, and PA molecules (Figure S21). Compared to BDOM500-Cd and BDOM700-Cd, BDOM300-Cd exhibits higher molecular unsaturation (with elevated (DBE-O)/C ratios) and greater aromaticity (indicated by lower AI_{mod} values) (Table S19). BDOM molecules with lower oxidation state (O/C) and higher saturation degree (H/C) are more susceptible to Cd binding, with Cd exhibiting greater selectivity towards O/C than H/C. To quantify these potential chemical reactions, we calculated the functional group difference in molecular formulae representing key reactions, such as demethylation and decarboxylation. Across all samples and reaction types, LG transformation events predominated quantitatively (Figures 4A-C), indicating that substantial LG molecules underwent modifications (e.g., functional group alterations, conformational changes, or direct Cd binding) while retaining their core categorical characteristics post-reaction. Additionally, LG consistently demonstrates partial conversion to PA and TN, predominantly through oxidation, demethylation, and decarboxylation pathways, revealing that a subset of LG molecules experienced more substantial chemical transformations during complexation. Oxygenation reactions demonstrated the broadest substrate and product diversity across all samples, while dealkylation reactions showed the highest degree of LP involvement. Deamination exhibited the lowest overall transformation frequency with relatively simple reaction pathways.

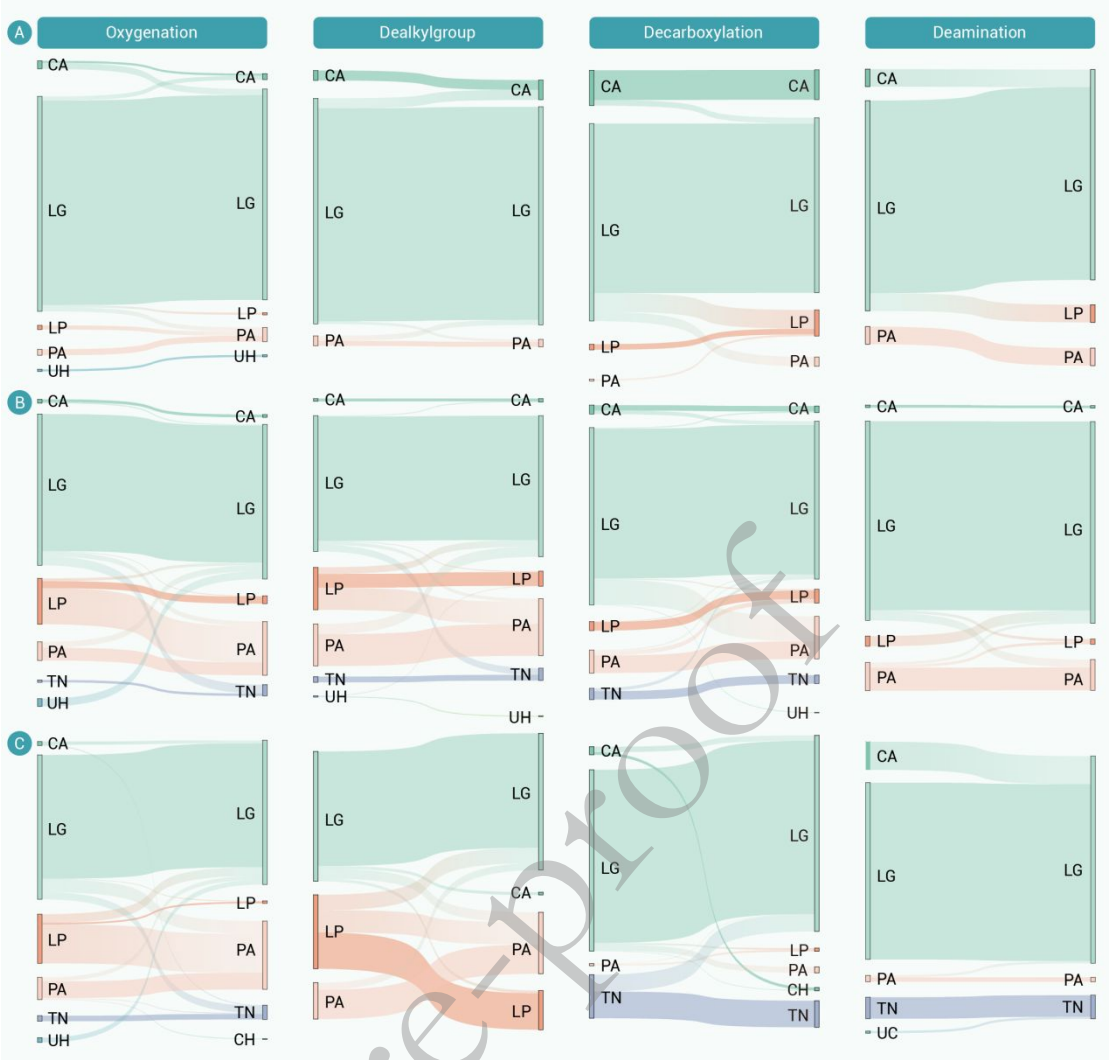

Figure 4 | Molecular transformations during Cd coordination (A-C) Possible chemical reactions occurring between different compound classes: oxygenation, dealkylation, decarboxylation and deamination between BDOM and BDOM-Cd molecules, and quantitative data for chemical reactions occurred among various compound classes is available in Table S22.

BDOM700 and BDOM500 demonstrate significantly higher molecular transformation activity compared to BDOM300, as evidenced by both the total number of transformation events and the diversity of reaction pathway (Figure 5A). Notably, BDOM700 and BDOM500 exhibits distinct patterns in their dominant transformation pathways. BDOM700 showed the highest conservation strength for LG during

decarboxylation (319 events), with particularly prominent transformations of TN through both conservative decarboxylation (49 events) and conversion to LG (31 events). The BDOM500-Cd system exhibits enhanced molecular transformations, particularly through oxygenation and dealkylation reactions. Despite its relatively lower Cd chelation capacity, BDOM500-Cd demonstrated elevated levels of strong-coordination ligands, LG content, and overall molecular conversion. This divergence may be attributed to the highly efficient and selective COOH coordination in BDOM700. Kendrick mass defect (KMD) analysis was applied to further examine the transformation and removal patterns of these compounds (Figures 5B & S22).[44] Many compounds differ solely in their functional groups while maintaining identical core structures at the same molecular level. In the KMD plot, molecules with higher carboxyl and amino group content predominantly distribute on the right side, while coordination-generated compounds clustered on the left and removed compounds dispersed toward the right. This distribution pattern indicates that Cd coordination induced decomposition of (oligo)-carboxyl and (oligo)-amino compounds, a phenomenon particularly pronounced in the BDOM700-Cd group.

The thermodynamic transformation pathways of BDOM, combined with molecular stability classification, collectively establish a hierarchical regulatory network for Cd coordination (Figures 5C-D & Tables S20-21).[45] In BDOM300, the thermochemical process was dominated by LG, yet their transformation was severely constrained by the recalcitrance of aromatic condensed structures (RA exhibited negligible LG content). The labile-active (LA) initially localized at LG (1699) and TN

(168) (Table S10), but post-chelating LA-LG depletion (1699-0) revealed a critical limitation: while low-temperature lignin retained incipient reactivity, its thermodynamic barrier (thermodynamically limited process (TLP)-LG, 57416) prevented effective coordination restructuring, resulting in recalcitrant-active/ recalcitrant-inactive (RA/RI) retention. Post-reaction, thermodynamically favorable process (TFP) declined to 20603 (66.8% reduction), with TLP-LG still accounting for 91.4% of residuals, conclusive evidence that untransformed lignin constitutes the primary bottleneck in chelation performance decay. In BDOM500, the TFP/TLP ratio increased to 1.07, reflecting enhanced thermodynamic activity within the system. Concurrently, the LG fraction in RA species rose significantly to 1790, indicating progressive structural reorganization. Notably, the emergence of LA-PA species signifies a pivotal transition: nitrogen-containing compounds now overcome inherent thermodynamic barriers, marking a critical advancement in reaction selectivity. Pyrolysis at 700℃ fundamentally altered the thermodynamic conversion landscape. The TN fraction in TFP increased to 16.5%, representing a 179% enhancement compared to BDOM300. Remarkably, TN maintained a high activity even after coordination. The RA-LG/RI-LG ratio reached 3.98, demonstrating that Cd coordination induced thermodynamically favorable rearrangement of recalcitrant LG fractions (Figure S23).

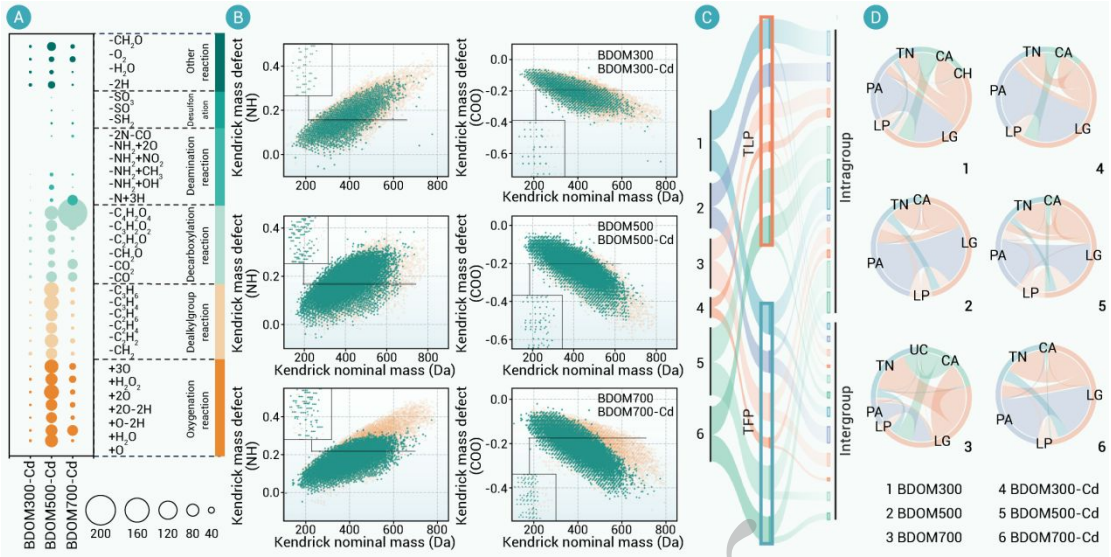

Figure 5 | Molecular and thermodynamic pathways during Cd coordination (A) The bubble diagrams shows the number of possible precursor-product pairs during the Cd chelation process. (B) KMD (COO) and (NH) during the Cd chelation process and its scale-expanded segments. (C) Sankey diagram showing the number of intragroup and intergroup thermodynamically favorable transformations (TFP) and thermodynamically limited transformations (TLP). (D) Chord diagram showing the specific intergroup transformations.

Core molecules tracking

To elucidate the transformation mechanisms of BDOM during Cd chelation, we systematically compared mass changes and molecular formula differences, identified and quantified potential reaction pathways, and constructed a correlation network analysis and phylogenetic trees for the reaction chains (Figure S24 & Table S23).[46] Based on this analysis, we selected the top 10 molecular formulas with the highest weights in each group and performed a mass difference network analysis on 119 reactions, effectively linking precursor-product pairs (Figure S25). BDOM300 follows a sequential reaction pathway, where $C_{17}H_{16}O_8$, $C_{17}H_{18}O_8$, and $C_{18}H_{18}O_8$ serve as precursors (Figure 6). The primary reaction is decarboxylation (–CO, $–CO_2$, $–CH_2O$, etc.), leading to the formation of fission intermediates, such as glyoxal ($–C_2H_2O_2$),

methylglyoxal ($–C_3H_4O_2$), and diacetyl ($–C_4H_6O_2$).[47] These intermediates then undergo aromatization and polymerization, forming unsaturated and aromatic compounds. Following, a sequential cascade reaction can be outlined as follows, starting with BDOM300 dealkylation, followed by a cascade of decarboxylation and dehydrogenation. The cascade reaction terminates at $C_{13}H_{14}O_6$, where, in addition to the aromatic ring structure, the C-O-C and -COOH form an effective chelation site for Cd. Higher pyrolysis temperatures stabilize the lignin molecular structure, making BDOM500 and BDOM700 groups more inclined to undergo a "one-step reaction" during chelation. In contrast, the transformation in BDOM500 is more complex, involving various processes such as decarboxylation, dehydration, oxidation, and aromatic ring cleavage, resulting in diverse free functional groups. The main products are $C_{11}H_{14}O_7$ and $C_{13}H_{16}O_6$, where $C_{13}H_{16}O_6$ and $C_{13}H_{14}O_6$ are considered homologous. In the BDOM700 group, the decarboxylation rate reached 34.62%, with the high carboxyl content in the precursors playing a pivotal role in this phenomenon. Notably, most of these -COOH groups were ester-linked, forming a distinctive "ester-carboxyl" motif. Given the inherent complexity and recalcitrance of lignocellulose, the selective activation and cleavage of such functional groups remained a longstanding challenge in the field.[48,49] However, the presence of ester bonds likely facilitates Cd-promoted selective scission. Specifically, the "ester-carboxyl" architecture likely exhibits enhanced susceptibility to cleavage, particularly in the presence of transition metals, especially when compared to isolated carboxyl groups.[50]

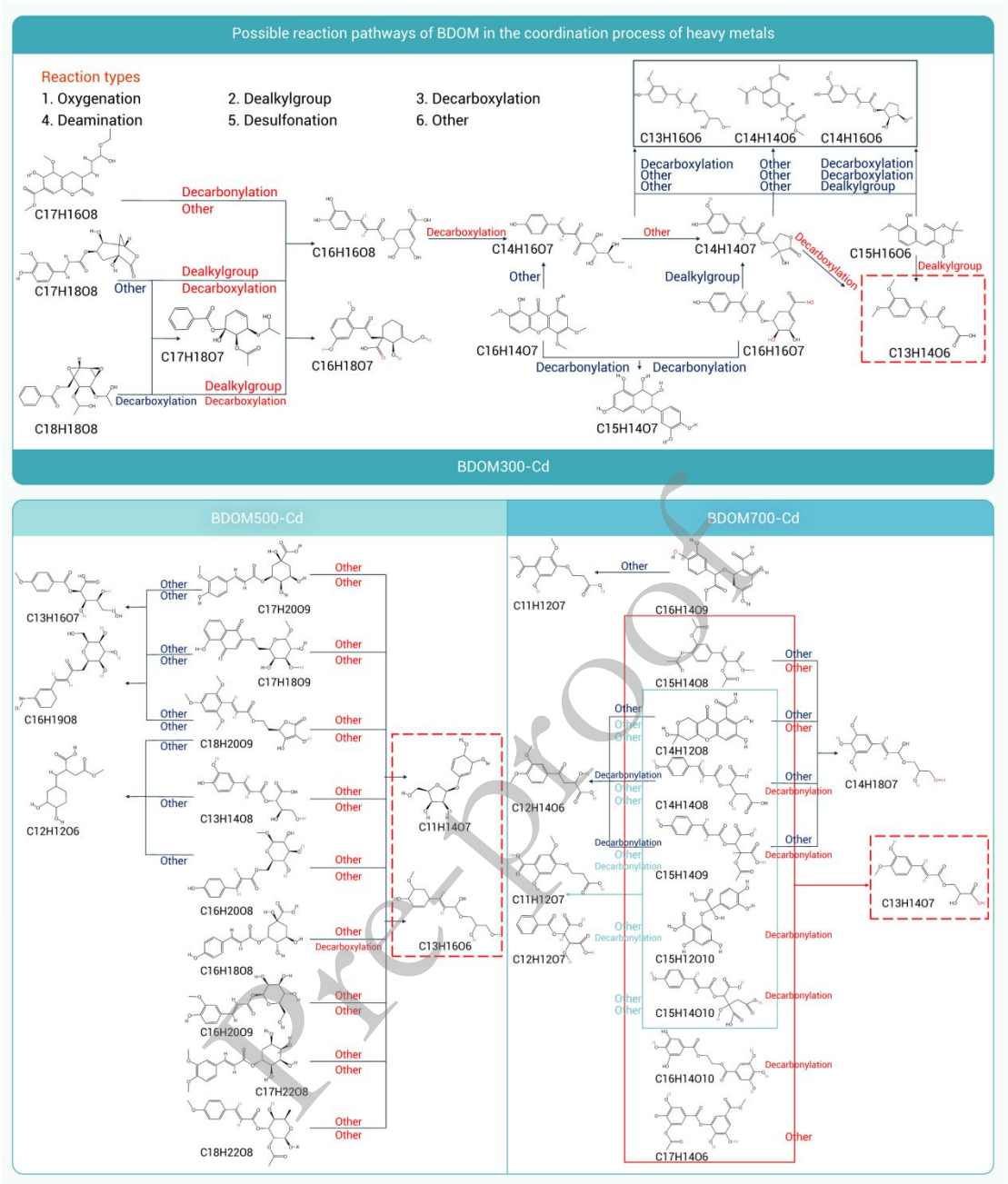

Figure 6 | Possible transformation pathways of BDOM during Cd chelation and the effect of pyrolysis temperature on BDOM formation.

Planting experiments to follow the Cd- mobilization/immobilization over the soil-plant interface

We selected ryegrass, a species known for its relatively high tolerance to Cd, as a model plant to evaluate the ecological effects of the BDOM-Cd molecular coordination in a soil-plant system (Methods S9-10 & Table S24).[51] The bioavailability of Cd in

soil, along with its uptake and translocation in plants, serves here as key indicators for assessing its environmental behavior. Sequential chemical extraction of soil Cd revealed that all BDOM treatments reduced the acid-extractable Cd fraction compared to the control group CK (same soil with Cd, but no BDOM), indicating the Cd immobilization potential of BDOM (Figure 7A-D). This immobilization effect increases significantly with increasing pyrolysis temperature ($P < 0.05$). While the reducible-Cd fraction exhibited only minor variations across treatments, the consistent increase in the oxidizable-Cd fraction supports our earlier hypothesis: high-temperature pyrolysis promotes the formation of a phenol-dominated molecular configuration in BDOM, which facilitates Cd stabilization in the organic-bound phase via synergistic coordination, thereby converting Cd from labile to stable forms.

The Cd translocation from soil to roots was assessed using the bioaccumulation factor: It quantifies that BDOM700 significantly inhibits translocation from soil to roots and the subsequent transfer to the leafs (Figure 7E-F). On the contrary, BDOM300 treatment led even to increased Cd accumulation in stems and leaves, suggesting that the loosely complexed Cd formed under low-temperature pyrolysis acts as a translocation factor and enhances Cd phytoavailability, likely because labile Cd-BDOM complexes remained more phytoavailable.

Cd phytotoxicity primarily arises from its ability to induce reactive oxygen species (ROS) overproduction, which triggers oxidative stress and cellular damage.[52] In the antioxidant defense system, peroxidase (POD), superoxide dismutase (SOD), and catalase (CAT) are key enzymes involved in ROS scavenging, membrane integrity

maintenance, and oxidative damage mitigation.[53] Enzyme activity assays showed that, compared to CK, BDOM300 did not significantly enhance POD or SOD activities, whereas BDOM700 increased their activities by 39.8% and 83.8%, respectively (Figure S26). Meanwhile, CAT activity was elevated by 15.3% and 35.6% in BDOM500 and BDOM700 treatments, respectively ($p < 0.05$), indicating that high-temperature BDOM effectively activates the antioxidant enzyme system in ryegrass, As a marker of membrane lipid peroxidation, malondialdehyde (MDA) content decreased by 12.5% under BDOM700 treatment, Cd-induced oxidative damage is alleviated by both the lower amount taken up as well as the stimulation of the enzymatic protection system.[54]

In terms of soil nutrient status and plant growth responses, BDOM application exerted positive effects on soil habitat health and promoted ryegrass leaf and root elongation. The dry and fresh weights increased by 26.0-87.0% and 92.4-235.5%, respectively, compared to the untreated Cd-containing soil CK ($p < 0.05$; Figure 7G & Figure S27) without BDOM. Previous studies have shown that Cd toxicity inhibits plant growth by disrupting root tip mitosis, inducing DNA damage and lipid peroxidation and interferes with the photosynthetic metabolism. Typical Cd toxicity symptoms-such as leaf curling, chlorosis, root malformation, and tissue necrosis-may occur when Cd accumulation exceeds 3-30 mg/kg.[55] The growth promotion observed in this study may be attributed to the effective suppression of Cd uptake and translocation by BDOM, including the impediment of Cd entry into root cytoplasm and xylem loading, as well as the reduction of Cd bioavailability in soil through speciation changes. These mechanisms collectively alleviate Cd phytotoxicity, thereby sustaining normal plant

metabolism and morphogenesis (Figure 7H).

The decrease in Cd phytoavailability associated with BDOM–Cd coordination was also accompanied by changes in the soil bacterial community. The Simpson index and PCoA results showed that CK, BDOM300, BDOM500 and BDOM700 were clearly separated from each other (Figure S28), indicating that the three BDOMs did not produce the same microbial response, although they were added at the same DOC level. LEfSe analysis further identified different discriminant bacterial groups along the pyrolysis-temperature gradient (LDA score > 3.0; Figure S29).

BDOM300 mainly enriched substrate-responsive taxa, including *Spirosomataceae*, *Dyadobacter, Pedobacter, Arcicella* and *Exiguobacterium.* Some of these groups are known to be involved in the utilization of dissolved organic substrates, polysaccharide turnover and environmental stress adaptation. This pattern agrees with the relatively high proportion of mobile and reactive molecules in low-temperature BDOM, as well as its weaker ability to stabilize Cd. In the BDOM500 treatment, the enriched taxa shifted toward actinomycete-related and stress-adapted groups, including *Streptomyces, Streptomycetaceae, Kitasatosporales* and *Neobacillus*, together with *Acetobacterales.* This suggests that, at the intermediate pyrolysis temperature, the microbial response was no longer dominated only by easily available carbon, but was also related to the processing of more transformed organic substrates and organic-acid-associated carbon metabolism.

In contrast, BDOM700 enriched several groups more closely related to root-zone functioning and metal-stress adaptation, including *Azospirillum, Rhizobium* and

Bacillales. *Magnetospirillum* and *Sphingobacteriales* were also enriched in this treatment; these groups are more often associated with redox- or Fe-mineral-related processes and organic substrate turnover. Such a microbial pattern is consistent with the stronger Cd coordination capacity of BDOM700 and the lower Cd transfer to ryegrass. Taken together, these results suggest that high-temperature BDOM not only stabilized Cd through stronger molecular coordination, but also favored a root-zone microbial environment associated with lower Cd bioavailability and improved plant stress adaptation.

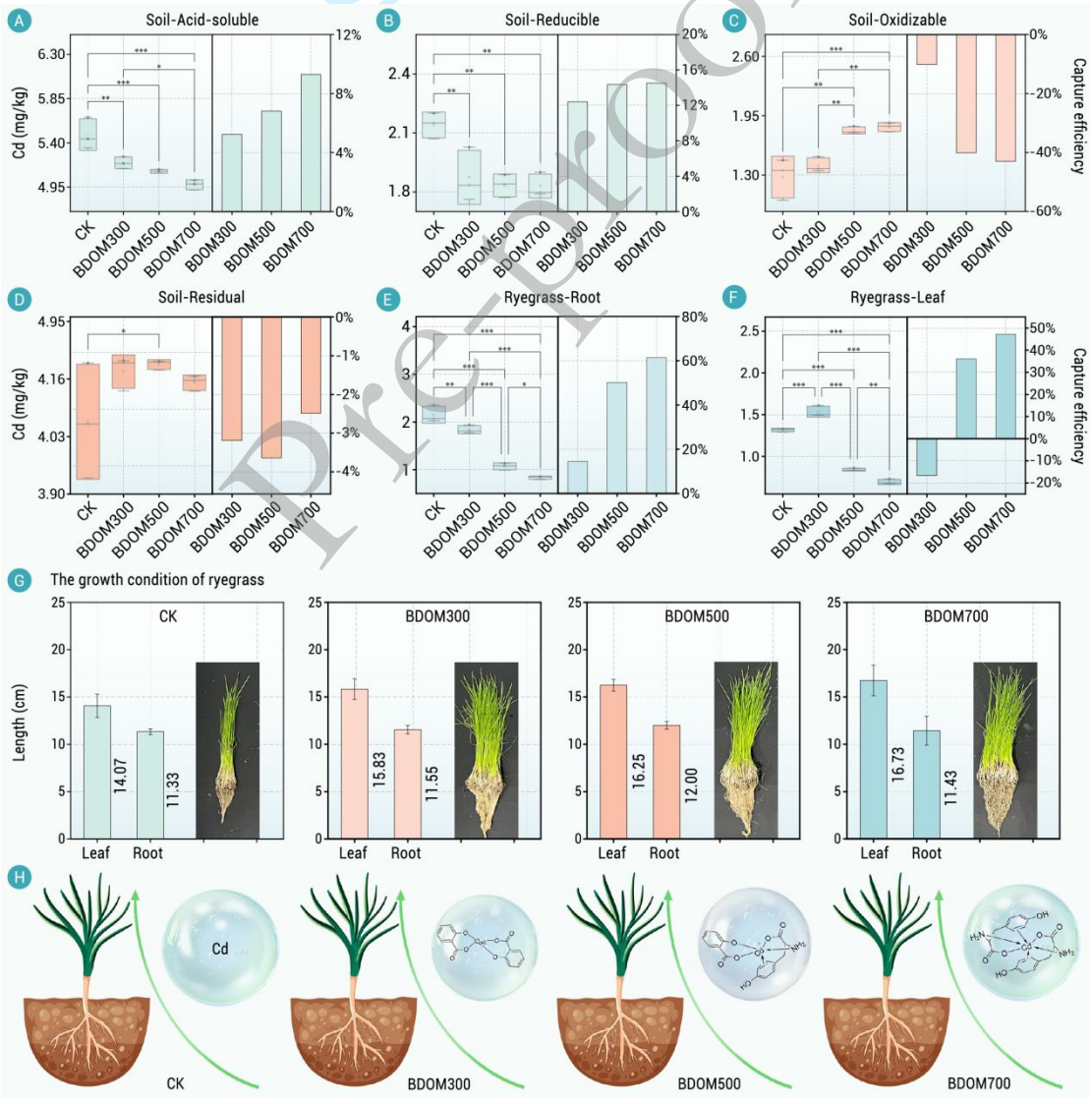

Figure 7 | BDOM immobilizes soil Cd and limits its uptake by ryegrass (A-D) The fraction

of Cd in soils. For each panel, the left side depicts the concentration of a specific Cd fraction (F1: acid-extractable, F2: reducible, F3: oxidizable, F4: residual) across treatments using box plots, with asterisks indicating significant differences compared to the CK group; the right side shows the corresponding capture efficiency. Cadmium concentration in ryegrass roots (E) and leafs (F). (G) Plant growth responses, including root length, shoot length, and representative photographic evidence. (H) A proposed schematic model illustrating the mechanism by which BDOM impedes cadmium uptake and translocation in plants.

CONCLUSION

This study focusses on the previously largely hidden molecular processes throughout the generation of a most relevant environmental material, biochar. The ongoing processes are analyzed by focusing to the question how pyrolysis temperature controls the molecular structure of BDOM, which is the molecular arm of biochar's active chemical functionality. More specifically, structural reorganization mechanisms due to metal coordination throughout the material condensation can also be followed, which hitherto influences the ability to immobilize heavy metals, here Cd as a model.

The findings address knowledge gaps in conventional biochar carbonization reaction models, which predominantly focus on bulk properties of solid-phase biochar while overlooking the essential functionality and its subsequent chemical reactivity in BDOM.[56] Integrated spectroscopic, mass spectrometric, and reaction network analyses demonstrate that elevated-temperature pyrolysis (700℃) drives dissociation of humic aggregates and targeted enrichment of phenolic components in local domains, thereby enhancing cadmium binding. This performance optimization arises from thermally induced topological rearrangement of functional groups optimizing their binding configurations, while nitrogen-containing molecules recombine into another

conjugated, electron-deficient subdomains, and hydrophobic microcavity encapsulation reinforces complex stability. These mechanistic insights resolve longstanding uncertainties regarding molecular reconfiguration during metal coordination-a dynamic process previously obscured by BDOM's extreme molecular heterogeneity, where thousands of compounds with different redox states, aromaticity, and functionalization coexist. Pyrolysis-driven directional transformations achieve a transition from a disordered polytype of binding sites to rather highly coordinated molecular microenvironments, with quantitative characterization of chemical pathways confirming that high temperatures select thermodynamically favorable molecular species where stabilization by metal ions or surfaces makes them recalcitrant. Most importantly for soil applications, this stable coordination effectively suppresses Cd translocation, thereby reducing its in-plant accumulation, as experimentally quantified in ryegrass plating tissues.

Overall, this work elucidates fundamental structure-function relationships between pyrolysis-induced molecular reorganization of biochars and BDOM-metal coordination behavior, especially advancing mechanistic understanding of BDOM-mediated contaminant immobilization. This in turn enables rationally designed bio-waste-based remediation materials tailored for specific environmental applications which are scalable, affordable, and sustainable.

REFERENCE

1. Yang H., Huang X. and Thompson J. R. (2015). Biochar: pros must outweigh cons. *Nature* **518**:483. DOI:10.1038/518483f
2. Cernansky R. (2015). Agriculture: state-of-the-art soil. *Nature* **517**:258–260. DOI:10.1038/517258a
3. Niu X., He Y., Musl O., et al. (2024). Bark extractives as sources of carbon-efficient functional precursors and materials. *Innov. Mater.* **2**:100074. DOI:10.59717/j.xinn-mater.2024.100074
4. Yu P., Zhang B., Zhang Y., et al. (2026). What's next in materials science? *Innov. Mater.* **4**:100196. DOI:10.59717/j.xinn-mater.2026.100196
5. Yu S., Lu Z., Chen L., et al. (2026). Electrically conductive wood-based materials beyond biochar: modifications, functions, and environmental impact. *Matter* **9**:102528. DOI:10.1016/j.matt.2025.102528
6. Kleber M., Bourg I. C., Coward E. K., et al. (2021). Dynamic interactions at the mineral–organic matter interface. *Nat. Rev. Earth Environ.* **2**:402–421. DOI:10.1038/s43017-021-00162-y
7. Yang F., Wang C. and Sun H. (2021). A comprehensive review of biochar-derived dissolved matters in biochar application: production, characteristics, and potential environmental effects and mechanisms. *J. Environ. Chem. Eng.* **9**:105258. DOI:10.1016/j.jece.2021.105258
8. Peng B., Li T., Guo Y., et al. (2025). The key components of biochar's environmental behavior and potential ecological risks: biochar-derived dissolved organic matter. *J. Water Process Eng.* **72**:107499. DOI:10.1016/j.jwpe.2025.107499
9. Smith C. R., Sleighter R. L., Hatcher P. G., et al. (2013). Molecular characterization of inhibiting biochar water-extractable substances using electrospray ionization Fourier transform ion cyclotron resonance mass spectrometry. *Environ. Sci. Technol.* **47**:13294–13302. DOI:10.1021/es4034777
10. Sun Y., Xiong X., He M., et al. (2021). Roles of biochar-derived dissolved organic matter in soil amendment and environmental remediation: a critical review. *Chem. Eng. J.* **424**:130387. DOI:10.1016/j.cej.2021.130387
11. Lyu H., Zhang H., Dong J., et al. (2024). Pyrolysis temperature matters: biochar-derived dissolved organic matter modulates aging behavior and biotoxicity of microplastics. *Water Res.* **250**:121064. DOI:10.1016/j.watres.2023.121064
12. Wang W., Nie M., Yan C., et al. (2024). Effect of pyrolysis temperature and molecular weight on characterization of biochar derived dissolved organic matter from invasive plant and binding behavior with the selected pharmaceuticals. *Environ. Pollut.* **348**:123867. DOI:10.1016/j.envpol.2024.123867
13. Masud M. A. A., Samaraweera H., Mondol M. M. H., et al. (2025). Iron biochar synergy in aquatic systems through surface functionalities electron transfer and reactive species dynamics. *npj Clean Water* **8**:46. DOI:10.1038/s41545-025-00471-5
14. Fan T., Yao X., Sun Z., et al. (2023). Properties and metal binding behaviors of sediment dissolved organic matter (SDOM) in lakes with different trophic states along the Yangtze River Basin: a comparison and summary. *Water Res.* **231**:119605.

DOI:10.1016/j.watres.2023.119605

15. Huang M., Li Z., Wen J., et al. (2021). Molecular insights into the effects of pyrolysis temperature on composition and copper binding properties of biochar-derived dissolved organic matter. *J. Hazard. Mater.* **410**:124537. DOI:10.1016/j.jhazmat.2020.124537
16. Fu H., Liu H., Mao J., et al. (2016). Photochemistry of dissolved black carbon released from biochar: reactive oxygen species generation and phototransformation. *Environ. Sci. Technol.* **50**:1218–1226. DOI:10.1021/acs.est.5b04314
17. Kind T. and Fiehn O. (2007). Seven golden rules for heuristic filtering of molecular formulas obtained by accurate mass spectrometry. *BMC Bioinformatics* **8**:105. DOI:10.1186/1471-2105-8-105
18. Bramer L. M., White A. M., Stratton K. G., et al. (2020). ftmsRanalysis: an R package for exploratory data analysis and interactive visualization of FT-MS data. *PLoS Comput. Biol.* **16**:e1007654. DOI:10.1371/journal.pcbi.1007654
19. Koch B. P. and Dittmar T. (2006). From mass to structure: an aromaticity index for high-resolution mass data of natural organic matter. *Rapid Commun. Mass Spectrom.* **20**:926–932. DOI:10.1002/rcm.2386
20. LaRowe D. E. and Van Cappellen P. (2011). Degradation of natural organic matter: a thermodynamic analysis. *Geochim. Cosmochim. Acta* **75**:2030–2042. DOI:10.1016/j.gca.2011.01.020
21. Patel S. A. and Erickson L. E. (1981). Estimation of heats of combustion of biomass from elemental analysis using available electron concepts. *Biotechnol. Bioeng.* **23**:2051–2067. DOI:10.1002/bit.260230910
22. Battley E. H. (1998). The development of direct and indirect methods for the study of the thermodynamics of microbial growth. *Thermochim. Acta* **309**:17–37. DOI:10.1016/S0040-6031(97)00357-2
23. Popovic M. (2019). Thermodynamic properties of microorganisms: determination and analysis of enthalpy, entropy, and Gibbs free energy of biomass, cells and colonies of 32 microorganism species. *Heliyon* **5**:e01950. DOI:10.1016/j.heliyon.2019.e01950
24. Liu L., Yang X., Ahmad S., et al. (2023). Silicon (Si) modification of biochars from different Si-bearing precursors improves cadmium remediation. *Chem. Eng. J.* **457**:141194. DOI:10.1016/j.cej.2022.141194
25. Chen W.-H., Wang C.-W., Ong H. C., et al. (2019). Torrefaction, pyrolysis and two-stage thermodegradation of hemicellulose, cellulose and lignin. *Fuel* **258**:116168. DOI:10.1016/j.fuel.2019.116168
26. Liu N., Dou C., Yang X., et al. (2025). Effects of pretreatment procedure, compositional feature and reaction condition on the devolatilization characteristics of biomass during pyrolysis process: a review. *J. Energy Inst.* **118**:101943. DOI:10.1016/j.joei.2024.101943
27. Zheng J., Kwak K., Chen X., et al. (2006). Formation and dissociation of intra–intermolecular hydrogen-bonded solute–solvent complexes: chemical exchange two-dimensional infrared vibrational echo spectroscopy. *J. Am. Chem. Soc.* **128**:2977–2987. DOI:10.1021/ja0570584
28. Xu S., Yang J., Su P., et al. (2024). Identifying key intermediates for the oxygen

evolution reaction on hematite using ab-initio molecular dynamics. *Nat. Commun.* **15**:10411. DOI:10.1038/s41467-024-54796-9

29. Wang S., Dai G., Yang H., et al. (2017). Lignocellulosic biomass pyrolysis mechanism: a state-of-the-art review. *Prog. Energy Combust. Sci.* **62**:33–86. DOI:10.1016/j.pecs.2017.05.004
30. Wang N., Zhi Y., Wei Y., et al. (2020). Molecular elucidating of an unusual growth mechanism for polycyclic aromatic hydrocarbons in confined space. *Nat. Commun.* **11**:1079. DOI:10.1038/s41467-020-14493-9
31. Ciccone V., Lin E., Prieto Kullmer C. N., et al. (2026). Double deoxygenative coupling of carboxylic acids and alcohols. *ACS Catal.* **16**:12645–12652. DOI:10.1021/acscatal.6c02684
32. Grandbois M., Beyer M., Rief M., et al. (1999). How strong is a covalent bond? *Science* **283**:1727–1730. DOI:10.1126/science.283.5408.1727
33. Gunina A. and Kuzyakov Y. (2022). From energy to (soil organic) matter. *Glob. Change Biol.* **28**:2169–2182. DOI:10.1111/gcb.16071
34. Freeman L. A., Walley J. E. and Gilliard R. J. (2022). Synthesis and reactivity of low-oxidation-state alkaline earth metal complexes. *Nat. Synth.* **1**:439–448. DOI:10.1038/s44160-022-00077-6
35. Liu X., Xi S., Kim H., et al. (2021). Restructuring highly electron-deficient metal-metal oxides for boosting stability in acidic oxygen evolution reaction. *Nat. Commun.* **12**:5676. DOI:10.1038/s41467-021-26025-0
36. Noda I. (2016). Two-dimensional correlation spectroscopy (2DCOS) analysis of polynomials. *J. Mol. Struct.* **1124**:53–60. DOI:10.1016/j.molstruc.2016.01.091
37. Yang H., Yang S., Kong J., et al. (2015). Obtaining information about protein secondary structures in aqueous solution using Fourier transform IR spectroscopy. *Nat. Protoc.* **10**:382–396. DOI:10.1038/nprot.2015.024
38. Wünsch U. J., Murphy K. R. and Stedmon C. A. (2017). The one-sample PARAFAC approach reveals molecular size distributions of fluorescent components in dissolved organic matter. *Environ. Sci. Technol.* **51**:11900–11908. DOI:10.1021/acs.est.7b03260
39. Tiwari J., Ramanathan A. L., Bauddh K., et al. (2023). Humic substances: structure, function and benefits for agroecosystems—a review. *Pedosphere* **33**:237–249. DOI:10.1016/j.pedsph.2022.07.008
40. Deng J.-H., Luo J., Mao Y.-L., et al. (2020). π-π stacking interactions: non-negligible forces for stabilizing porous supramolecular frameworks. *Sci. Adv.* **6**:eaax9976. DOI:10.1126/sciadv.aax9976
41. Ellerbrock R. H. and Gerke H. H. (2021). FTIR spectral band shifts explained by OM–cation interactions. *J. Plant Nutr. Soil Sci.* **184**:388–397. DOI:10.1002/jpln.202100056
42. Mackie A. L., Park Y. and Gagnon G. A. (2022). Calibration of high performance size exclusion chromatography (HPSEC) for molecular weight estimation of aquatic humic substances. *J. Environ. Chem. Eng.* **10**:108913. DOI:10.1016/j.jece.2022.108913
43. Terkhi M. C., Taleb F., Gossart P., et al. (2008). Fourier transform infrared study of mercury interaction with carboxyl groups in humic acids. *J. Photochem. Photobiol. A Chem.* **198**:205–214. DOI:10.1016/j.jphotochem.2008.03.018
44. Hughey C. A., Hendrickson C. L., Rodgers R. P., et al. (2001). Kendrick mass defect

spectrum: a compact visual analysis for ultrahigh-resolution broadband mass spectra. *Anal. Chem.* **73**:4676–4681. DOI:10.1021/ac010560w

45. Cheng Z., Hu Q., Guo H., et al. (2024). Long-term straw return enhanced the chlorine reactivity of soil DOM: highlighting the molecular-level activity and transformation trade-offs. *Sci. Total Environ.* **951**:175485. DOI:10.1016/j.scitotenv.2024.175485
46. Cai S., Zhang Y., Hu A., et al. (2023). Dissolved organic matter transformation mechanisms and process optimization of wastewater sludge hydrothermal humification treatment for producing plant biostimulants. *Water Res.* **235**:119910. DOI:10.1016/j.watres.2023.119910
47. Homoki-Farkas P., Örsi F. and Kroh L. W. (1997). Methylglyoxal determination from different carbohydrates during heat processing. *Food Chem.* **59**:157–163. DOI:10.1016/S0308-8146(96)00273-7
48. Sulis D. B., Lavoine N., Sederoff H., et al. (2025). Advances in lignocellulosic feedstocks for bioenergy and bioproducts. *Nat. Commun.* **16**:1244. DOI:10.1038/s41467-025-56472-y
49. Ren W., Zhang D., Zhou Y., et al. (2024). Lignin's complex role in lignocellulosic biomass recalcitrance: a case study on bamboo. *Chem. Eng. J.* **490**:151422. DOI:10.1016/j.cej.2024.151422
50. Mohan V., Naske C. D., Britten C. N., et al. (2020). Hydroxide-catalyzed cleavage of selective ester bonds in phosphatidylcholine: an FTIR study. *Vib. Spectrosc.* **109**:103055. DOI:10.1016/j.vibspec.2020.103055
51. Ma H., Wei M., Wang Z., et al. (2020). Bioremediation of cadmium polluted soil using a novel cadmium immobilizing plant growth promotion strain Bacillus sp. TZ5 loaded on biochar. *J. Hazard. Mater.* **388**:122065. DOI:10.1016/j.jhazmat.2020.122065
52. Mahmud J. A., Hasanuzzaman M., Nahar K., et al. (2018). Insights into citric acid-induced cadmium tolerance and phytoremediation in Brassica juncea L.: coordinated functions of metal chelation, antioxidant defense and glyoxalase systems. *Ecotoxicol. Environ. Saf.* **147**:990–1001. DOI:10.1016/j.ecoenv.2017.09.045
53. Ke T., Guo G., Liu J., et al. (2021). Improvement of the Cu and Cd phytostabilization efficiency of perennial ryegrass through the inoculation of three metal-resistant PGPR strains. *Environ. Pollut.* **271**:116314. DOI:10.1016/j.envpol.2020.116314
54. Hu T., Li H.-y., Zhang X.-z., et al. (2011). Toxic effect of NaCl on ion metabolism, antioxidative enzymes and gene expression of perennial ryegrass. *Ecotoxicol. Environ. Saf.* **74**:2050–2056. DOI:10.1016/j.ecoenv.2011.07.013
55. Li Q., Xing Y., Huang B., et al. (2022). Rhizospheric mechanisms of Bacillus subtilis bioaugmentation-assisted phytostabilization of cadmium-contaminated soil. *Sci. Total Environ.* **825**:154136. DOI:10.1016/j.scitotenv.2022.154136
56. Liu R., Liu G., Yousaf B., et al. (2022). Novel investigation of pyrolysis mechanisms and kinetics for functional groups in biomass matrix. *Renew. Sustain. Energy Rev.* **153**:111761. DOI:10.1016/j.rser.2021.111761

FUNDING AND ACKNOWLEDGMENTS

This study was funded by the Outstanding Youth Project of Heilongjiang Province (JQ2024D001). The Excellent Master's/Doctoral Thesis Program of Heilongjiang Province (59010010). The funders had no role in study design, data collection and analysis, decision to publish, or preparation of the manuscript.

AUTHOR CONTRIBUTIONS

Y.L. conceived and designed the study. X.M. conducted the experiments. S.A. analyzed the data. M.A. provided conceptual guidance. F.Y. supervised the project. K.C. revised the manuscript. All authors approved the final manuscript.

DATA AND CODE AVAILABILITY

Data are available from the corresponding author upon reasonable request.

DECLARATION OF INTERESTS

Markus Antonietti is an Editorial Board member of The Innovation Materials and was blinded from reviewing or making final decisions on the manuscript. Peer review was handled independently of this member and their research group. The other authors declare no conflicts of interest.

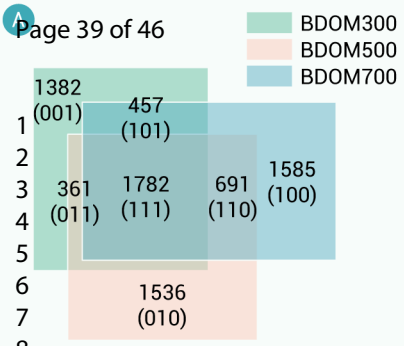

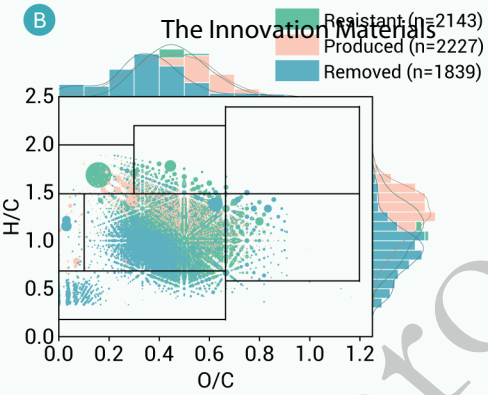

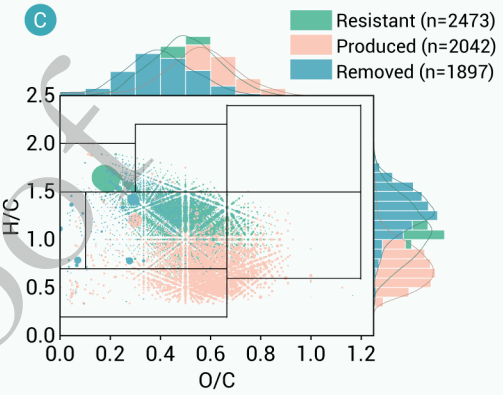

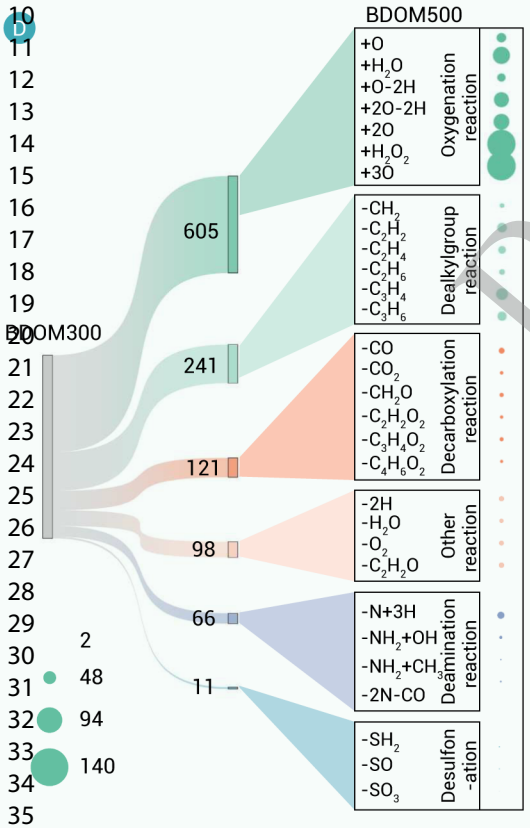

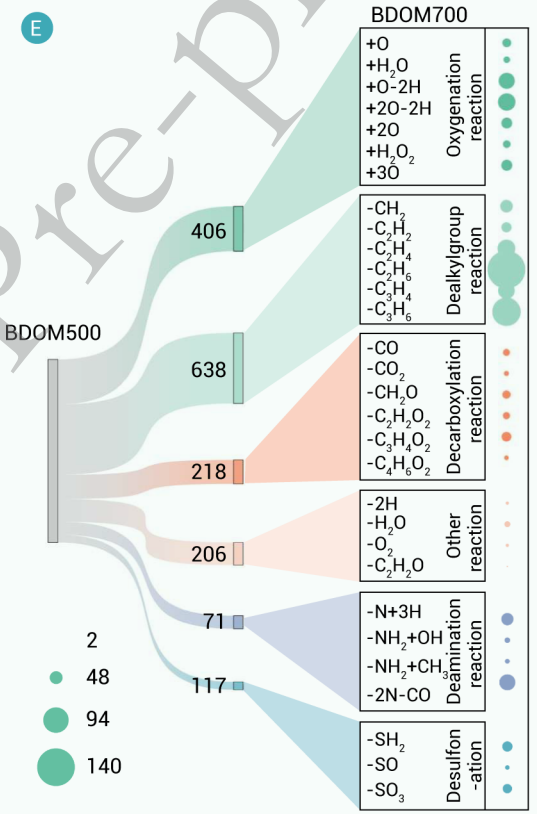

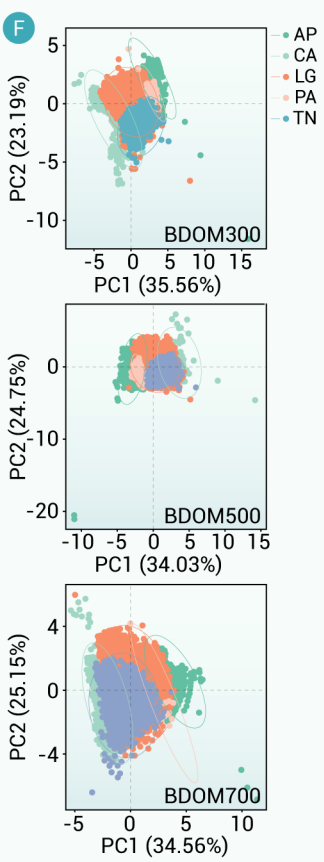

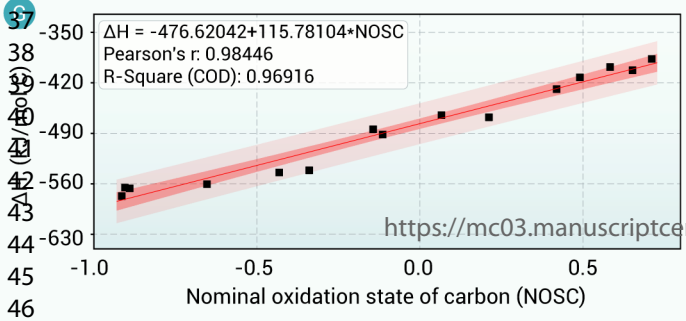

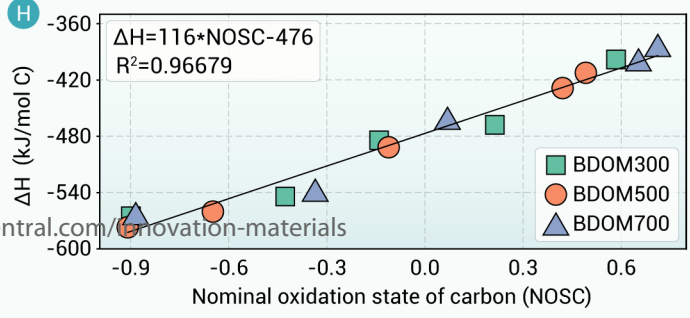

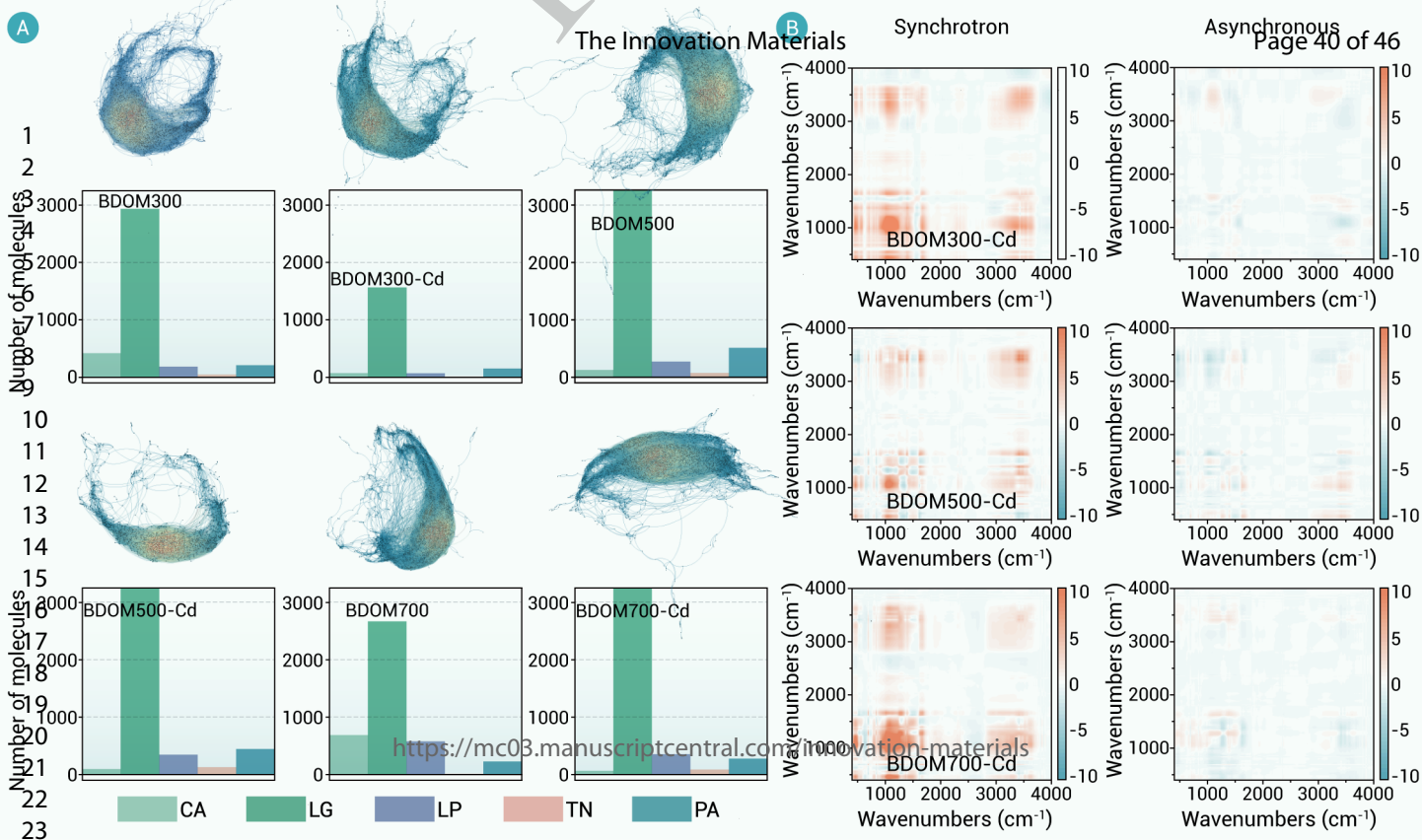

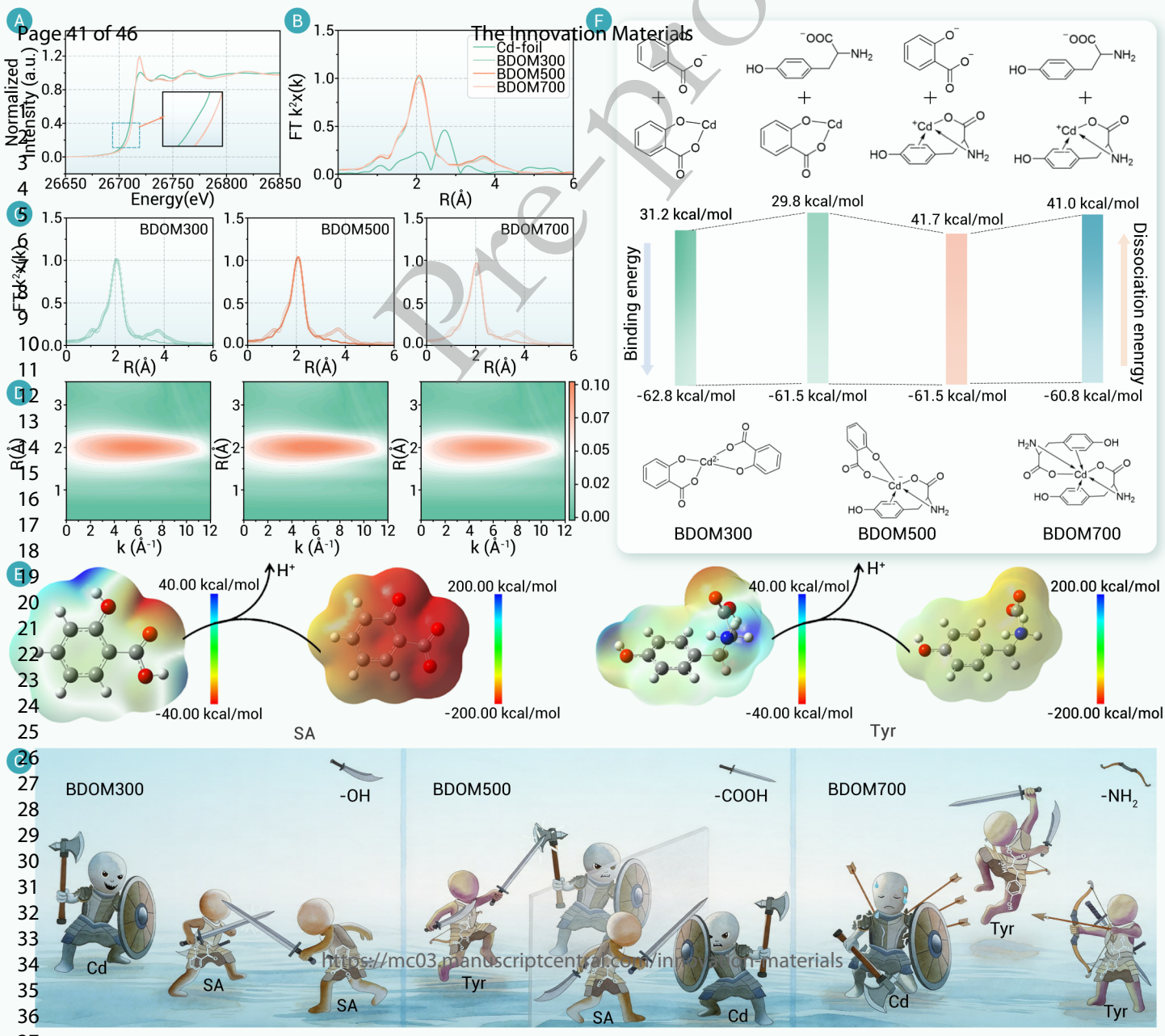

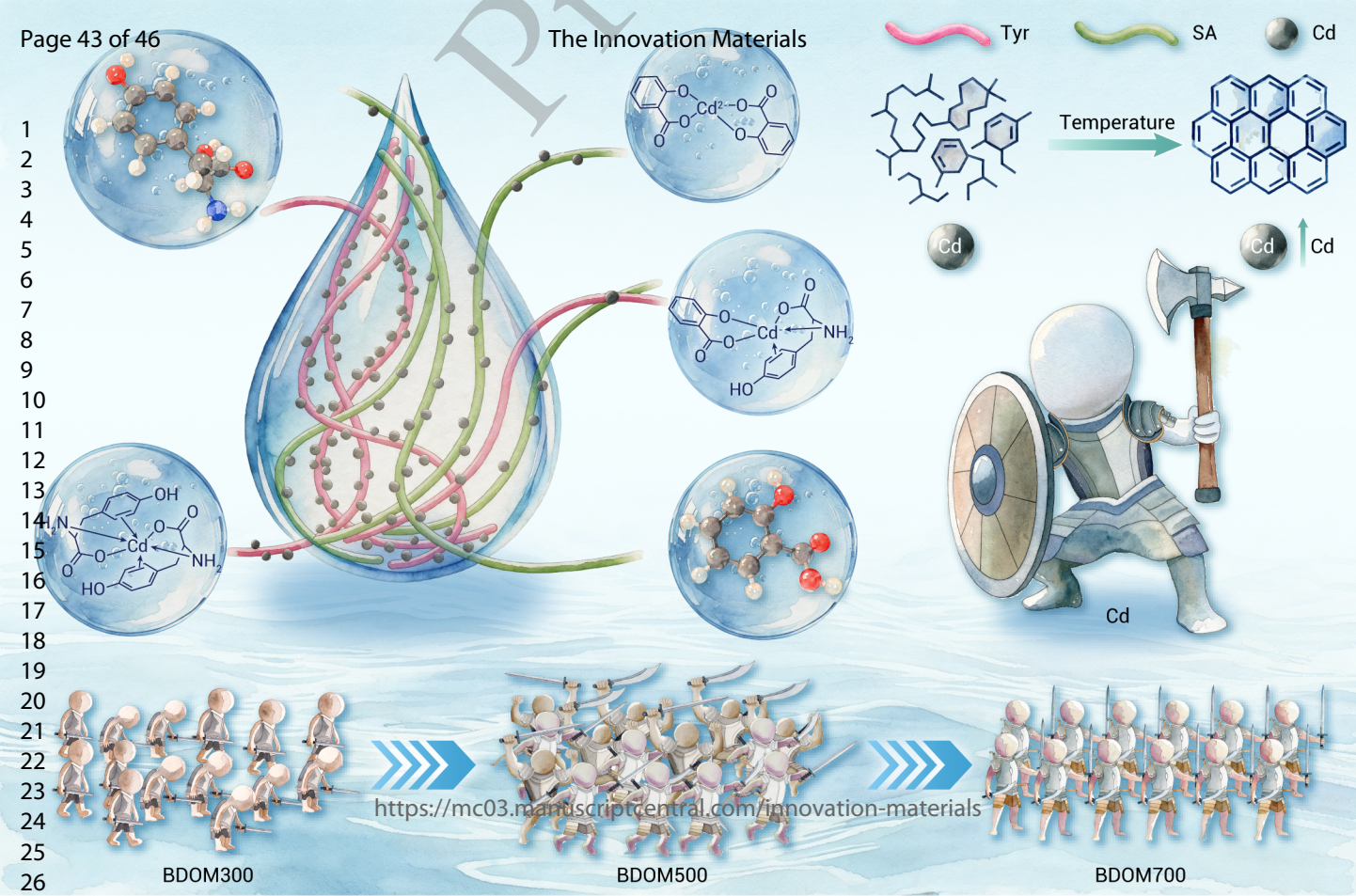

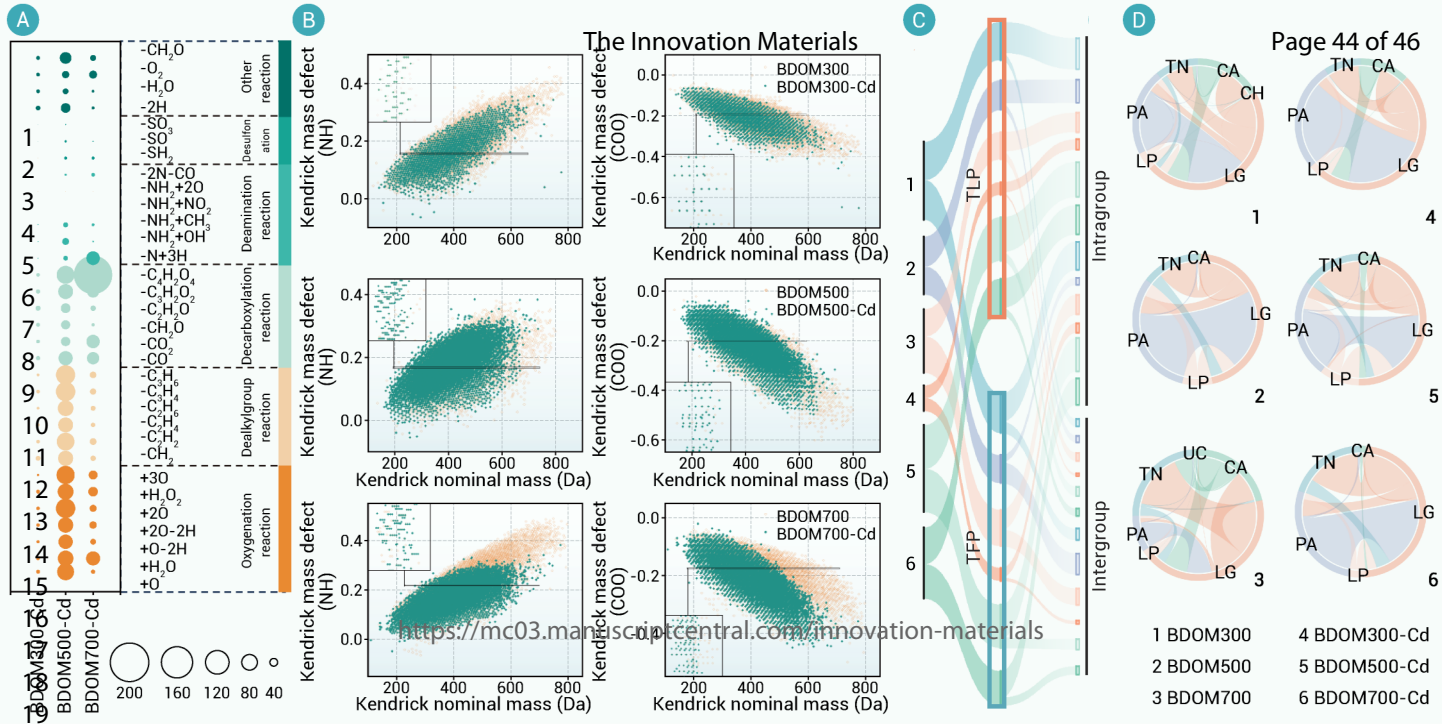

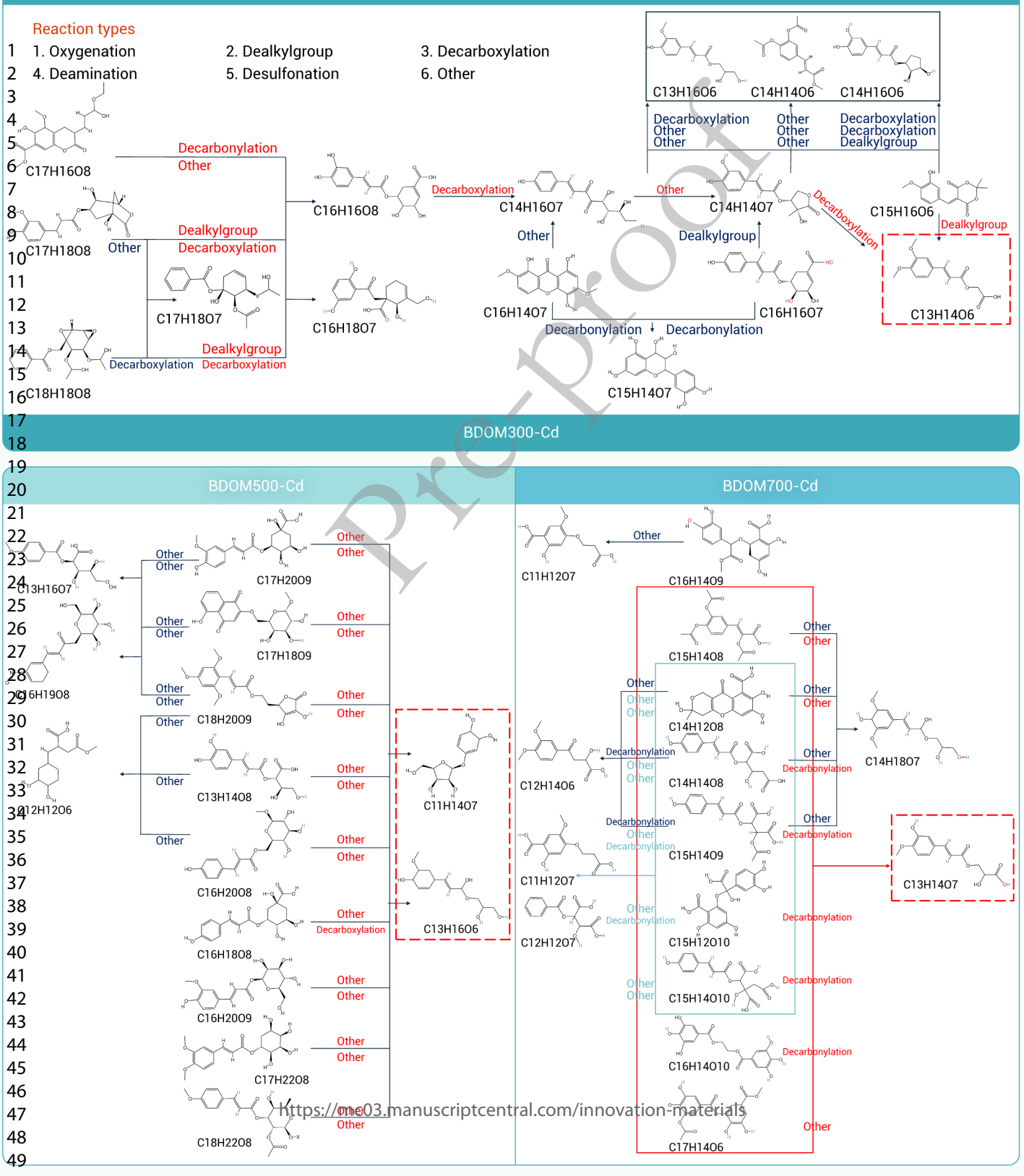
Possible reaction pathways for biochar-mediated detoxification process of heavy metals
Reaction types
1. Oxygenation
2. Dealkylgroup
3. Decarboxylation
4. Deamination
5. Desulfonation
6. Other
C17H16O8
C17H18O8
C18H18O8
C16H16O8
C17H18O7
C16H18O7
C14H16O7
C14H14O7
C16H14O7
C16H16O7
C15H14O7
C13H16O6
C14H14O6
C14H16O6
C15H16O6
C13H14O6
BDOM300-Cd
BDOM500-Cd
C13H16O7
C16H19O8
C12H12O6
C17H20O9
C17H18O9
C18H20O9
C13H14O8
C16H20O8
C16H18O8
C16H20O9
C17H22O8
C18H22O8
C11H14O7
C13H16O6
BDOM700-Cd
C11H12O7
C16H14O9
C15H14O8
C14H12O8
C14H14O8
C12H14O6
C15H14O9
C11H12O7
C12H12O7
C15H12O10
C15H14O10
C16H14O10
C17H14O6
C14H18O7
C13H14O7
Other
Decarbonylation
Decarboxylation
Dealkylgroup
https://mc03.manuscriptcentral.com/innovation-materials
Pre-proof